Astron. Astrophys. 243, 118–138 (1991)

ASTRONOMY AND ASTROPHYSICS

N-body code for simulation of planar disk-disk encounters: application to tidally triggered bar formation

H. Salo [1,2]

[1] Observatory and Astrophysics Laboratory University of Helsinki, SF-00130 Helsinki, Finland
[2] Department of Astronomy, University of Oulu, SF-90570 Oulu, Finland

Received February 14, accepted September 11, 1990

Abstract. A new method for 2-dimensional simulations of galaxy encounters is introduced. The simulation system consists of two planar particle disks embedded in rigid spherical halos. In addition to stellar component reacting solely to gravitational forces, gaseous component is included by allowing for dissipative impacts between some of the particles. The new feature of the model is in the calculation of the gravitational potential: this is performed simultaneously in two moving, mutually overlapping logarithmic polar coordinate systems, attached to the centers of each halo. Polar coordinates are used only for potential calculations, the integrations for particles as well as for halo centers being carried out in an inertial rectangular system. The advantage of this method lies on the fact that due to the use of two polar coordinate systems the resolution of the potential calculation is always greatest in the regions where particle density is highest, whereas integrations can be performed by using simple and fast cartesian leapfrog methods. Also, when using a logarithmic grid, it is very easy to cover a large region by a rather limited number of cells, so that there is practically no limitations for the distance between the systems. However, both disks must lie on the orbital plane. In future the code will be applied to systematic survey of gravitationally induced activity in galaxies. Some preliminary results concerning tidal triggering of stellar bars and their effects on the gaseous component are presented.

Key words: numerical methods – active galaxies – kinematics and dynamics – spiral galaxies

1. Introduction

Nowadays there exists a wealth of data suggesting connection between galaxy-galaxy gravitational interactions and the different kinds of star formation and nuclear activity manifested by them. This has been demonstrated by statistical studies of large samples of close pairs as well as by detailed studies of individual strongly interacting systems (e.g. Dahari 1984, 1985; Kennicutt & Keel 1984; Joseph & Wright 1985; Cutri & MacAlary 1985; Bushouse 1987). However, the connections are all but simple: for example there seems to be no clear dependence between the mutual separation of the systems and the level of activity shown by them. In fact, not even those close pairs with clear morphological signs of tidal features always display excess activity, whereas some signs of excess activity can sometimes be observed also in samples of galaxies extending to large mutual separations (Laurikainen & Moles 1989). This implies that there must be a large number of factors governing the response of systems to tidal perturbations. These probably include, in addition to the strength and geometry of the external perturbation, for example the internal dynamical state of the galaxy as well as the amount of gas and its distribution before the encounter. Also, possible mass transfers between the components might in some cases have importance.

This paper represents a first phase of study aiming to address the connection between the dynamics of galaxy encounters and the different types of induced activity. In order to achieve this goal, a new *N*-body code has been constructed, including both the stellar and gaseous components of the galaxies. Therefore, in addition to the previously well-studied tidal phenomena induced in the mass distribution of the systems, we can also get a handle to the behaviour of gas, and thus to the probable distribution of recent star formation regions, more closely related to the apparent luminosity distribution of the systems. The choice of the simulation method is based on the desire to be able to perform systematic surveys of as many different model parameters as possible. We shall, therefore, limit our attention to 2-dimensional encounters of disk systems, and exclude mergings. In the present paper the simulation method is described, together with some results concerning the conditions necessary for the formation of tidally induced stellar bars. This problem was considered to be extremely important, since bars are very efficient in changing the angular momentum distribution of gas component, thus for example enabling the large-scale gas infall to the nuclear regions, offering a source of energy to active nuclei (see e.g. Noguchi 1988).

Two-dimensional particle-mesh codes offer a fast method for surveys of the dynamical evolution of essentially flat disk systems. Gravitational potential arising from the disk particles is typically calculated in rectangular or polar coordinate grids, by employing FFT-methods. Halos are treated as an inert component, based on the fact that due to their large random velocities they should react only weakly to perturbations. However, this assumption is based on simulations of isolated systems (see Sellwood 1981) and it is somewhat unclear how well justified it is in the case of external perturbations. Anyway, once the potential is constructed, by adding disk potential and rigid halo component, forces can be calculated by various interpolation schemas. The CPU time consumption in both the force calculation, and the integration of particle orbits scales proportionally to N, making it possible to reach easily up to $N = 10^4$–10^5 or even more particles. Typically, in accordance with the approximativeness of force calculations,

only simple second-order integration methods are used. The advantage of using cartesian grids lies on the fact that very fast explicit leapfrog methods can be used for orbit advancement. Also, application of FFT is very straightforward, as well as extensions to 3-dimensions. On the other hand, polar grids offer much better resolution in the central parts of the system, and are thus very efficient when simulating centrally condensated planar systems like disk galaxies. Therefore, smaller total number of mesh points is needed to cover the area of interest with a necessary resolution. However, there are disadvantages in using polar coordinates: for example, special treatment is necessary in the center of the coordinate system. Also, in typical polar methods (e.g. Miller 1976), implicit leapfrog schemas are needed.

The simplest way to study galaxy interactions is to replace the perturbing system by a point mass while the other system possesses a full particle disk (e.g. Byrd et al. 1986; Sundelius et al. 1987). In this case the perturbing potential can simply be added to the self-gravitational potential of the disk and the rigid halo component at the mesh area, thus causing only insignificant extra CPU-time consumption as compared to study of isolated disks. However, if both systems are to possess a full disk simple polar methods are not practical, and cartesian grids covering both systems are usually applied. Since a large area must then be covered with equally sized bins, resolution becomes inevitably rather poor.

The present study describes a method for simulations of two disks, which tries to combine the advantages of both cartesian and polar grids. The new feature concerns the tabulation of gravitational potential: this is performed with two moving, mutually overlapping polar grids, whose centers are attached to centers of the two halos. For each particle coordinates are calculated with respect to both grids, while its mass is assigned only to one grid. The logaritmic polar grid method of Miller (1976) is used for both grids separately after which forces from both grids are added together. Thus the good resolution is retained near the centers of the both systems. However, orbital calculations, both for particles and halo centers, are performed in cartesian coordinate system, thus allowing the use of fast explicit leapfrog integration. Since logarithmic grids can cover large areas with very limited number of mesh points, there is no restrictions on the distance between interacting systems: large initial separations can be used, thus assuring that systems have time to settle into steady state before tidal forces start to influence their dynamics.

In addition to stellar disks, gaseous component is also included, by allowing a certain fraction of particles to represent gas clouds experiencing dissipative impacts. In contrast to typical treatment in N-body simulations where collisions are assumed to take place whenever two clouds fall into a same "collisional bin", here the orbits are followed to the exact location of impact, as is commonly done in collisional simulations of, say, planetary rings (Brahic 1977; Hämeen-Anttila & Lukkari 1980; Salo 1985, 1987; Wisdom & Tremaine 1988). This makes it possible to follow to greater accuracy, for example, the formation of shock fronts when the gas of two galaxies collides. Also, for the sake of completeness a simple model is included to mimic the star-formation cycles, largely following the model of Roberts & Hausman (1984) and Noguchi (1988), where cloud-cloud collisions produce stellar associations which after certain lifetime explode as supernovae and affect the motions of nearby clouds, thus partially feeding back kinetic energy lost in impacts. Future studies will concentrate on refining this aspect of the code.

The new code is described to some detail in Sects. 2 and 3, covering the treatment of stellar disks and gas clouds, respectively. In Sect. 4 results concerning the tidal triggering of stellar bars are presented, while Sect. 5 briefly discusses the behaviour of gas. Finally, Sect. 6 gives a few examples of the more realistic two disk runs.

2. Simulation system

The simulation system consists of two planar disks embedded in rigid spherical halos. The disk movement relative to each others is confined to the common plane of the disks. Various initial density models can be used for the disks as well as for the spherical halos. Optionally, a single isolated disk can be simulated, or a disk perturbed by a point mass or by any arbitrary spherical mass distribution. Both stars and gas clouds exert gravitational forces, but if desired, either of them or both can be treated as massless test particles. The treatment of clouds differs from that of stars in the sense that they can collide dissipatively. Alternatively, they can also be treated as another stellar component, possessing for example different initial distributions or random velocity dispersions as compared to ordinary stars. This enables two-component runs, for example for the studies of relaxation problems. All the different combinations are possible for each galaxy separately. The aim has thus been to produce a method as versatile as possible, to be used for various problems without need for major modifications.

In addition to stars and gas clouds a third category of particles, representing ballistically moving newborn stellar associations (OB-particles hereon) can be followed, assumed to be formed as a consequence of star forming cloud-cloud collisions. However, this crude and possibly grossly misleading inclusion of astrophysical processes should not be taken too literally. Rather, OB-particles can be considered simply as a convenient way of tracing where collisions predominantly take place. Therefore, their distribution is proportional to the square of the gas density. As demonstrated by Larson (1987) several possible accretion mechanisms for the formation of massive molecular clouds might lead to approximatively same type of proportionality between star formation rate and gas density.

2.1. *Equations of motion*

Since there is no special advantage in choosing either of the moving halos as the center of the coordinate system, orbital integrations are carried out in an inertial coordinate frame. The equations of motion for 2 halos and N particles can then be written down as:

$$\ddot{\boldsymbol{R}}_k = -\sum_{j=1}^{N} m_j \boldsymbol{F}_k(\boldsymbol{r}_j - \boldsymbol{R}_k) - M_{3-k}\boldsymbol{F}_{3-k}(\boldsymbol{R}_{3-k} - \boldsymbol{R}_k),\ k = 1,2, \qquad (1)$$

$$\ddot{\boldsymbol{r}}_j = \sum_{\substack{i=1 \\ i \neq j}}^{N} m_i(\boldsymbol{r}_i - \boldsymbol{r}_j)/[(\boldsymbol{r}_i - \boldsymbol{r}_j)^2 + \varepsilon^2]^{3/2} + \sum_{k=1}^{2} M_k \boldsymbol{F}_k(\boldsymbol{r}_j - \boldsymbol{R}_k), \quad j = 1, N. \qquad (2)$$

Here the radius vectors of particles are denoted by $\boldsymbol{r}_j$ while $\boldsymbol{R}_k$ stand for the halos, their masses being m_j and M_k, respectively. Softening length is denoted by ε, and the vector $\boldsymbol{F}_k$ represents the radial force function (acceleration per unit halo mass) due to halo k, $\boldsymbol{F}_k = -1/M_k \nabla \Phi_k$. The units have been fixed by setting the gravitational constant G into unity.

It is evident that the assumption of halos moving rigidly is anything but correct. Also the use of the same force function $\boldsymbol{F}_k$ for the halo-particle and halo-halo interaction is only an approximation. These and other model restrictions are addressed below. However, in the case of point-mass perturber the above formulation in terms of moving halos is totally equivalent to the typical method (see e.g. Sundelius et al. 1987) where a rigid halo is assumed and its center is fixed at the origo of the coordinate system, while both direct and indirect perturbations are included.

2.2. *Force calculations*

The practical way of constructing the self-gravitational forces in the righthand side of Eqs. (2) is to use the polar grid method, deviced by Miller (1976) for an isolated disk. Here this method is applied to the two disks separately, and since there is little difference in the details of the calculations, only a brief summary is given.

The potential grid is defined by coordinates u and v,

$$R = R_{\text{cent}} \exp \alpha u, \qquad 0 < u \leqq N_R, \tag{3}$$

$$\phi = \alpha v, \qquad 0 \leqq v \leqq N_\phi - 1, \tag{4}$$

where R and ϕ are the polar coordinates with respect to the halo center, and $\alpha = 2\pi/N_\phi$, where N_ϕ denotes the number of azimuthal mesh points. In radial direction the mesh extends over N_R cells, while R_{cent} stands for the radius of the central hole in the grid. Due to the logarithmic nature of the grid, each mesh-box is approximatively square, and the relative resolution at each distance is constant, determined by N_ϕ: the box size corresponding to unit increment in u and v is $\Delta R/R = \Delta\phi = 2\pi/N_\phi$. On the other hand N_R determines the relative extent of the grid: $R_{\text{grid}}/R_{\text{cent}} = \exp(2\pi N_R/N_\phi)$. In Miller's original simulations fixed values $N_\phi = 36$, $N_R = 24$ were used, implying $R_{\text{grid}}/R_{\text{cent}} \approx 60$.

In the calculation of the potential, a density table is constructed by assigning mass of each particle to the nearest mesh point (NGP assignement). The selfgravitational potential of the disk at each grid point is then obtained by double summation over the grid, performed with the help of discrete Fourier transform (see Miller 1976). Once the potential due to disk is obtained, the rigid halo potential is added, being pre-tabulated at the beginning of the run. The forces due the total potential are calculated with the original 9-point interpolation formula of Miller.

Extra treatment is needed for particles falling outside the potential mesh. In previous simulations particles falling outside grid are simply ignored, or advanced by using forces calculated with more approximate methods, whereas particles entering the "grid hole" are moved through it by some analytical approximation (Miller 1976; Sundelius et al. 1987). However, we have chosen to calculate forces on all the particles with the same accuracy: the forces for both interior and exterior particles due to disk are obtained by direct summation. By using grid large enough in radial direction, number of particles requiring extra treatment can be kept very small, so that this means insignificant extra CPU time consumption. On the other hand the fact that all particles are treated in the same manner simplifies and considerably speeds up the integration of particle orbits. Actually, the number of particles falling outside the grid (or two grids, see below) can be kept to strictly zero, while only a few particles at each step fall inside the central hole. In order to achieve this, we have used values of R_{cent} which are of the order of $5\ 10^{-3}$ times the initial disk radius. Since this is an order of magnitude smaller than typical values of softening length, the resolution of the potential calculation close to the center is at least two orders of magnitude better than is actually needed! However, grid extending this close to origo offers very convenient means for the interpolation of forces and therefore optimizes total time consumption, including potential calculations, force interpolation, and orbital integrations.

The advantage of the polar method over rectangular potential evaluation is evident. Since the systems studied are centrally concentrated, density assignement and potential resolution as well as force interpolation are most accurate at the region where the density and self-gravitational effects are largest. However, in the case of two disks one polar mesh is clearly unsuitable.

This method has been extended to the simulation of two disks in a simple but efficient manner (see Fig. 1). For each particle we calculate its coordinates with respect to not only one but both halo centers, and construct two density and potential tables. Mass of each particle is assigned to the disk where it belongs to in the beginning of the simulation. Radial and tangential force contributions from both disk+halo systems are interpolated at the particle location in the same manner as before, and added together to yield total forces in a cartesian coordinate system were integrations are carried out. This method of course requires that the two grids overlap, but this is easily achieved with logarithmic grids. For example if we choose $N_R = 48$, $N_\phi = 36$, the relative extent of the grids is $R_{\text{grid}}/R_{\text{cent}} \approx 4000$. If the disk radii are of the order of unity and $R_{\text{cent}} = 0.005$, this means that separations of at least 20 disk radii can be handled, without extra treatment of external particles. It is easy to see that the arguments for the good resolution in the single disk case are still valid.

In addition to particles, one must move the halos in a consistent way. This is done as follows. The forces due to the disk belonging to the halo in question are calculated by summing over the disk density array. Typically, this back-action of the disk is very small (it vanishes in the axisymmetric case, and has apparently been altogether ignored in previous simulations), but is here included for the sake of completeness. The force due to the other halo and disk is calculated in the same manner as on any ordinary particle, by interpolating from the potential grid of the external system. This assures that halo centers and disks move coherently. However, treating halo centers and particles in similar manner can cause inaccuracy: in the case of non-identical halo potential models for the two systems, the forces between halos are not strictly equal, since they do not take into account the extended nature of both mass distributions simultaneously but simply replace one in turn with a mass point. Therefore, conservation of momentum is not fulfilled unless the halos are far from each other. Similar problems concern the calculation of particle-halo interaction, softened particles corresponding to small Plummer sphere halos with scale length of the order of ε. In general, the separation between halo centers must be at least 2–3 times that of the larger scale length in order to ensure symmetrical forces.

Other limitations for the method follow from the assumption of rigid spherical halos. For example, the tidal distortions of halos are not taken into account so that the overall potentials remain generally rounder than they should. Also, the amount of dynamical friction is underestimated, since only disks can convert orbital energy into random motions. Here, without detailed comparisons to fully self-consistent methods it is hard to estimate the significance of these inaccuracies. Nevertheless as long as close encounters are excluded these problems as well as that of unbalanced halo-halo forces should not be too severe.

2.3. *Orbital integrations*

Although polar grids are used for force evaluation, integrations are carried out in cartesian coordinates. In each step we have to

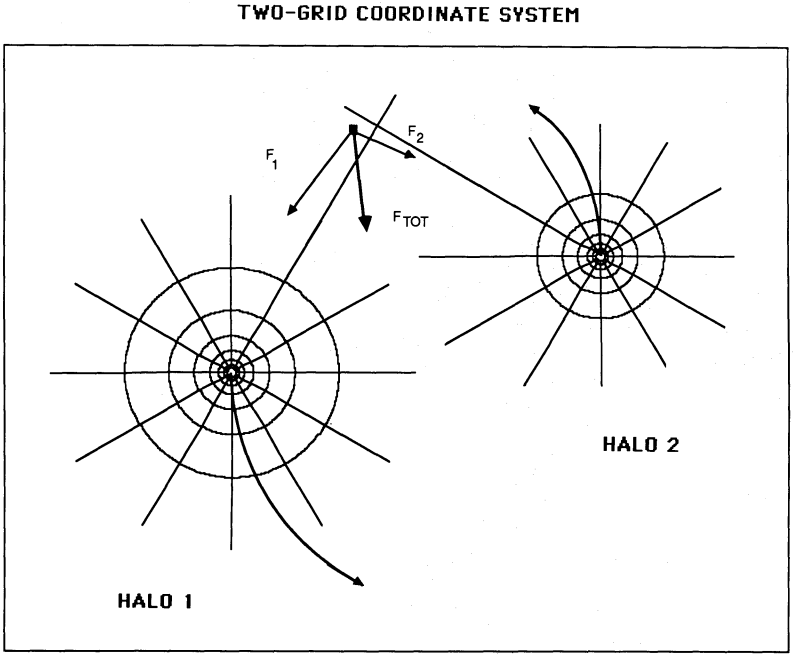

Fig. 1. Schematic representation of the 2-grid coordinate system used in the simulations. Two moving, logarithmic polar-coordinate grids, attached to the centers of the halos, are used in the potential calculations and force interpolations, while the equations of motion (both for halos and the particles) are integrated in the cartesian center-of-mass coordinate system. Actual overlapping grids used have 36 azimuthal and 48 radial gridpoints, thus extending over 20 disk radii. Forces on the few particles crossing the "central holes" are calculated separately, by summing over density distributions in the grid areas

make two transformations, from rectangular positions x, y of each particle into u_k, v_k, the logarithmic polar coordinates with respect to grids $k=1$ and 2, and then from polar force components $\partial\Phi_k/\partial u_k$ and $\partial\Phi_k/\partial v_k$ to cartesian forces F_x and F_y,

$$F_x = -\sum_{k=1}^{2} 1/\alpha r_k^2 \,(x_k \partial\Phi_k/\partial u_k - y_k \partial\Phi_k/\partial v_k), \tag{5}$$

$$F_y = -\sum_{k=1}^{2} 1/\alpha r_k^2 \,(y_k \partial\Phi_k/\partial u_k + x_k \partial\Phi_k/\partial v_k), \tag{6}$$

where x_k, y_k, and r_k stand for the cartesian components and radial distance with respect to halo center k. This disadvantage of back and forth transformations is more than outweighted by the fact that simple explicit time-centered leapfrog schema can be used, accurate to the second order in the time-step.

2.4. *Initial conditions*

In the present code one can choose between several possible surface density distributions for the disk, as well as between various halo potentials, yielding rotational velocity curves of different characteristics. So far we have concentrated on the Kuzmin disk (Toomre Model I) with the surface density

$$\Sigma(R) = aM_\infty/2\pi\,(R^2+a^2)^{-3/2}, \qquad 0<R \tag{7}$$

where M_∞ is the total mass of the disk and a is a scaling factor. The potential corresponding to this model is (Sellwood 1981)

$$\Phi(R) = -GM_\infty/a\,(1+R^2/a^2)^{-1/2}, \tag{8}$$

For the halo potential, one can use the same model (R is now a 3-dimensional radial coordinate), in which case Eq. (8) becomes the so called Plummer model with total mass M_∞ and Plummer radius a (hereon denoted by b). The theoretical rotational curve due to Kuzmin models has a rising part close to center, reaches its maximum slightly past the distance a and then gradually declines (see Sect. 4). In simulations truncated Kuzmin disks ($0<R<R_{\rm disk}$) will be used, and the simulation length unit will be determined by setting the truncation radius $R_{\rm disk}=1$. The fractional mass, $1-a/(1+a^2)^{1/2}$ falling outside $R_{\rm disk}$ will be redistributed inside $R_{\rm disk}$. Similarly, halo mass $M_{\rm halo}$ will denote the mass of the Plummer sphere within $R_{\rm disk}$, $M_{\rm halo}=M_\infty(1+b^2)^{-3/2}$.

In setting up the initial conditions the desired surface density distribution is represented in terms of a finite number of particles. In order to suppress unrealistically large random fluctuations, positions are typically assigned in some regular fashion. As in Miller's original code this is achieved by putting particles into regular rings, N_ϕ particles in each, the separations between rings reflecting the surface density law (each radial is located at the center of mass distance of the mass increment it represents). However, since a certain fraction of particles represents colliding gas clouds, they have a finite size assigned to them. In order to avoid overlapping in the initial state, typically in the inner- and the outermost parts of the disk, a slightly different method of setting up initial positions for gas clouds is used. Therefore, for gas particles not N_ϕ but some integer multiple KT times N_ϕ particles are placed in each ring. The factor KT is chosen in such a manner that tangential separations are as close as possible but smaller than radial separations between rings. The fact that KT is integer assures the initial symmetry of density also in the case gas particles possess mass. However, for self-gravitating gas the use of $KT>1$ will introduce high-order components into the overall density distribution which must be filtered out in the solution for potential.

The construction of initial velocities is realized by giving each ring a certain circular velocity and then adding random velocities for each particle. There are at least two different ways of determining appropriate circular velocities. One can either calculate them from the theoretical total potential, $V_{\rm circ}=(R\partial\Phi/\partial R)^{1/2}$, or calculate them self-consistently from the actual density distribution and the forces calculated by the method described in Sect. 2.2. These two methods, however, yield a slightly different $V_{\rm circ}$, partly due to finite number of particles and the approximative interpolation of forces, partly due to the softening used.

Although small, the difference if uncompensated, would be large enough to make any model out of equilibrium. Therefore, if analytical description is preferred, one must calculate a correction potential just balancing the difference between theoretical and actual velocity curves. This correction potential is then added to the rigid halo potential and is applied throughout the simulation. For example, Byrd et al. (1986) and Sundelius et al. (1987) take this approach. In the present code, no correction potential is used, but instead $V_{\rm circ}$ is constructed in a selfconsistent way, as in Sellwood (1981). This choice is largely a matter of taste, and no tests have been carried out to check if this makes any significant difference on the evolution of the system. However, when calculating velocities selfconsistently from the created particle positions, one can also use surface density models, for which no simple analytical potential models exist. For example, in some runs gas particles might have a constant surface density in some annular region.

The amount of random velocities is determined by specifying the value of the Toomre stability parameter,

$$Q_T = \kappa\sigma_r/3.36\,\mathrm{G}\Sigma, \tag{9}$$

where κ is the epicyclic frequency (calculated from the actual distribution) and σ_r the radial velocity dispersion. Random velocities are assumed to be normally distributed, and the ratio of radial and tangential velocity dispersions is calculated from the epicyclic approximation,

$$\sigma_r/\sigma_t = 2\Omega/\kappa. \tag{10}$$

The circular velocities are correspondingly corrected for the pressure support by random velocities, by the procedure of Ostriker & Peebles (1973), also applied by Sundelius et al. (1987).

The above described setting up of the initial conditions is always performed for both disks separately, before mutual gravitational interactions between disks are taken into account. In joining the two systems, their relative movement must be specified. At the moment the code allows for arbitrary hyperbolic (or parabolic) encounter between the systems. The geometry is defined by specifying the pericenter distance and velocity, together with the moment of time this is achieved. Normal celestial mechanical methods are used, involving the solution of hyperbolic Kepler-equation, by replacing the total masses of both systems with point masses placed at their centers. Therefore, actual closest distances and velocities, as well as the time when this occurs, differ slightly from those initially specified, partly due to the initially extended distribution of masses, partly due to the gravitational interaction between systems.

3. Collisional processes

The simplest way to incorporate gas dynamics and dissipative processes in N-body codes is to let particles experience partially inelastic collisions. This can be realized with various degrees of exactness. One can take the attitude that since the model is artificial and the particles in every case have unphysical dimensions, it is unnecessary to calculate individual impacts with any great precision. Accordingly various particle grid methods are employed: for example Schwartz (1984), Thomasson (1987), Combes & Gerin (1985) allow during each step every particle in the same rectancular bin to collide if they are approaching each other. Collisional frequency must then be scaled separately. On the other hand, Noguchi &Ishebashi (1986), Noguchi (1988) use a more accurate method by checking at each step for overlapping particles and making these collide, with the restriction that only one impact/cloud/step is allowed. Enough small stepsize must be used in order to assure that not too many impacts are missed. However, even this method is not very reliable if gas cloud number density is high, or if they have large streaming velocities.

The present code takes an altogether different approach, in using a method which aims to find every impact in its precise location, with the full accuracy provided by the leapfrog integrator. Partly this is done for aesthetic reasons to avoid potentially dangerous simplifications when possible, partly because in this manner the code has many potential applications in simulations of predominantly collision governed systems, like planetary rings. Also if the gas clouds were to possess different radii this would automatically ensure proper relative frequencies of impacts between different size groups.

In order to see the effects of dissipative processes each particle representing gas must, in average, experience several impacts during the simulation. If the total number of steps is limited due to CPU time consumption in force calculations for stellar population, it is necessary that several impacts take place during a single dynamical step. For example, if 1000 dynamic steps are taken while, say 5000 gas clouds are studied, 10 impacts/cloud/simulation would require about a total of 25 impacts/step. In the state of quiet evolution, most of the impacts take place between different clouds in altogether different locations of the systems, so that the problem of one cloud experiencing multiple impacts in one step is not severe. However, if shocks are produced, or if gas disks merge, most of the collisions occur in very localized areas. Therefore, some particles will collide very frequently, and it is hard to avoid missing impacts if one particle is allowed to collide only once during each dynamical step. An ideal solution would seem to be to be able to account for several impacts/step, not only between separate particles but for one particle. Due to simplicity of the leapfrog scheme this is indeed rather easy to achieve.

The standard leapfrog integrator is equivalent to second-order expansion

$$\boldsymbol{R}(t) = \boldsymbol{R}(0) + \boldsymbol{V}(-DT/2)\,t + 1/2\,\boldsymbol{F}(0)\,t\,(t+DT) \qquad 0 < t < DT, \tag{11}$$

$$\boldsymbol{V}(t) = \boldsymbol{V}(-DT/2) + \boldsymbol{F}(0)\,(t+DT/2), \tag{12}$$

which gives the correct positions at the endpoints of the time interval ($t = 0$ and $t = DT$) and correct velocity in the middle (the beginning of the timestep has been taken as a reference point). Let's assume that the particle experiences a velocity change $\Delta\boldsymbol{V}$ at the instant $0 < t^* < DT$, when its position is $\boldsymbol{R}^* = \boldsymbol{R}(t^*)$ and precollisional velocity $\boldsymbol{V}^* = \boldsymbol{V}(t^*)$. In terms of its initial values in the beginning of the time step, this is equivalent to transformation

$$\boldsymbol{R}(0) \rightarrow \boldsymbol{R}(0) - \Delta\boldsymbol{V}t^*, \tag{13}$$

$$\boldsymbol{V}(-DT/2) \rightarrow \boldsymbol{V}(-DT/2) + \Delta\boldsymbol{V}, \tag{14}$$

as can be verified by inserting these modified values into expansions (11) and (12). Therefore, we can account for a collision during the time step merely by changing the initial position and velocity before performing leapfrog. If there were several velocity changes during the step, they could all be simultaneously included by making successive transformations to $\boldsymbol{R}(0)$ and $\boldsymbol{V}(-\mathrm{DT}/2)$. This fact enables convenient calculation of multiple impacts of one gas particle during a single dynamical step.

In the present simulations, a simple impact model retaining the identity of the colliding clouds has been studied. In this model, the perpendicular component of the relative velocity of the impacting

clouds is reversed and its magnitude is decreased by a factor k, the coefficient of restitution. Conservation of linear and angular momentum then determines the changes of velocities of individual particles (Salo 1987),

$$\Delta V_1 = -\mu_2/\mu_1 \, \Delta V_2 = \mu_2/(\mu_1+\mu_2)\,(1+k)\; V_{\rm rel} \cdot CC, \qquad (15)$$

where $C = (R_2 - R_1)/(\sigma_1 + \sigma_2)$ is the unit vector in the direction joining the centres of the colliding particles, while σ_1, σ_2, μ_1 and μ_2 stand for their radii and masses, respectively, and $V_{\rm rel} = V_2 - V_1$ for the precollisional relative velocity. It is clear that this model in no way approximates the real behaviour of colliding molecular clouds, where the actual outcome might rather be a coalescence or fragmentation of impacting clouds than partially inelastic rebound, depending on the amount of the gravitational binding energy as compared to postcollisional kinetic energy. In future, more realistic models, based for example on the hydrodynamical simulations of molecular cloud collisions (Latanzio & Henriksen 1988) should be studied.

In practice the search of impacts is done as follows. In the beginning of each step gas particles are arranged according to the, say, increasing x-coordinate. All pairs of clouds residing closer than a certain minimum distance are picked up, and for these selected pairs, potential collisions are checked for by approximating the relative orbits with the parabolic approximation, Eq. (11). If impact is found possible during the step, the event is stored. Impact with smallest time is performed, and calculated changes in velocity are used to modify the initial positions and velocities of the clouds in question. Also, all entries involving either one of the just collided clouds are removed from table of potential collisions, and are replaced with new impact times, possibly with different particles than before, calculated from modified initial values [Eqs. (13) and (14)]. Only collisions occurring after the just performed impact are accepted. In this manner the continuously modified collision table is searched through, until no more potential collisions are left for that step. After this leapfrog is performed.

Although the above method works adequately in the case of a single gas disk, overlapping of gas disks requires some special attention. In this case, multiple impacts are not the only problem, but also the fact that the relative velocities between clouds are not determined by random velocity dispersion, but depend more on the systematic velocity difference between the two systems. Therefore, quadratic approximation of impact distance is poor, if large steps are used. For this reason, the time-step for gas particles (and OB-particles) can be made smaller than for the stellar population. In doing this we calculate the potential only once for every DT, although forces are always interpolated with appropriate positions.

The above procedure is probably unnecessarily accurate in the present context of galaxy encounters, but as was stated is useful if the same code is applied for purely collisional simulations. However, in future some faster methods will be investigated, and more attention will be paid on mimicking the actual physical processes.

4. Tidally triggered stellar bars

During a close interaction between two disk galaxies the mutual perturbations induce tidal deformations in both the stellar and gaseous components of the systems. Typically the bridge and tail features produced are sharper in the gas but otherwise fairly similar, being essentially determined by the direct impulsive tidal force exerted during the closest passage. On the other hand, the long term evolution is governed by the self-gravity of the systems and by the gas hydrodynamics, and can differ significantly for gas and stars. As pointed out by the simulations of Noguchi (1987, 1988; see also Noguchi & Ishebashi 1986) the behaviour of gas depends strongly on whether or not bar is formed in the stellar component. If this happens, large amounts of gas can be transferred into nuclear regions, thus offering at least qualitative support for the suggested connection between interactions and nuclear activity.

The first application of the 2-disk N-body code has been to study similar problems as addressed by Noguchi in his simulations with point-mass perturber. We have started a systematic survey of different factors affecting the tidal triggering of bars and the subsequent evolution of gas. These factors include the initial rotation curve, disk-halo mass ratio, strength and geometry of the perturbation, initial distribution as well as the properties assigned to gas. Here only preliminary results are reported: in fact most of the simulations described concentrate on the evolution of single disk perturbed by point-mass satellite, and on the stellar population, whereas only a few examples of the gas behaviour are shown. This seems to be a logical first step, since these results can then be applied to estimate what happens in the case of two realistically modeled disks, where the number of free parameters is much larger, and the mass transfer between systems might also be important in some cases. However, one must keep in mind that present simulations are strictly 2-dimensional, which probably affects the results. Also, realistic modeling of any particular observed pair can not be attempted.

Two kind of plots will be used in studying the bar formation: the projections of the particle distributions, and plots of the time behaviour of the bar rotation rates and axial ratios. The latter is done by calculating the principal axis of inertia for particle populations after every 10 time steps. This is done separately for the sub-systems of particles residing inside 0.25, 0.50, and 1.0 initial disk radii. In cases where clear rigidly rotating bars form this gives rather reliable estimates for the rotation rate, as well as for the shape of the bar feature, although in the case of weak features, the axial ratios deduced are closer to unity than what one would estimate for example by inspecting the projected outlook of the system. In any case, although this simple method does not give as much information as a detailed Fourier-component analysis (see e.g. Sellwood 1989), it should clearly distinct between systems where bar-like features form and systems which remain more or less axially symmetric.

4.1. *Choice of the galaxy model*

In order to study tidally triggered bar formation one must first construct an initially stable galaxy model, remaining axially symmetric in the case of no perturbation, and having meaningfully long 2-body relaxation time-scale. We have chosen to study the truncated Kuzmin disk embedded in Plummer halo, defined by Eqs. (7) and (8). This choice was based on two reasons. Firstly, Sellwood (1981) has studied bar formation in detail with these models, and his simulations offer suitable test material for the present simulation method (see Fig. 2). More importantly, by varying the parameters a and b, a large variety of rotation curves can be constructed in a systematic way. If $a = b$ both components yield similarly shaped potential in the disk plane.

There are two main ways how bar formation can be prevented in the case of an isolated galaxy: one can either increase the random velocity dispersion, or decrease the active self-gravitating

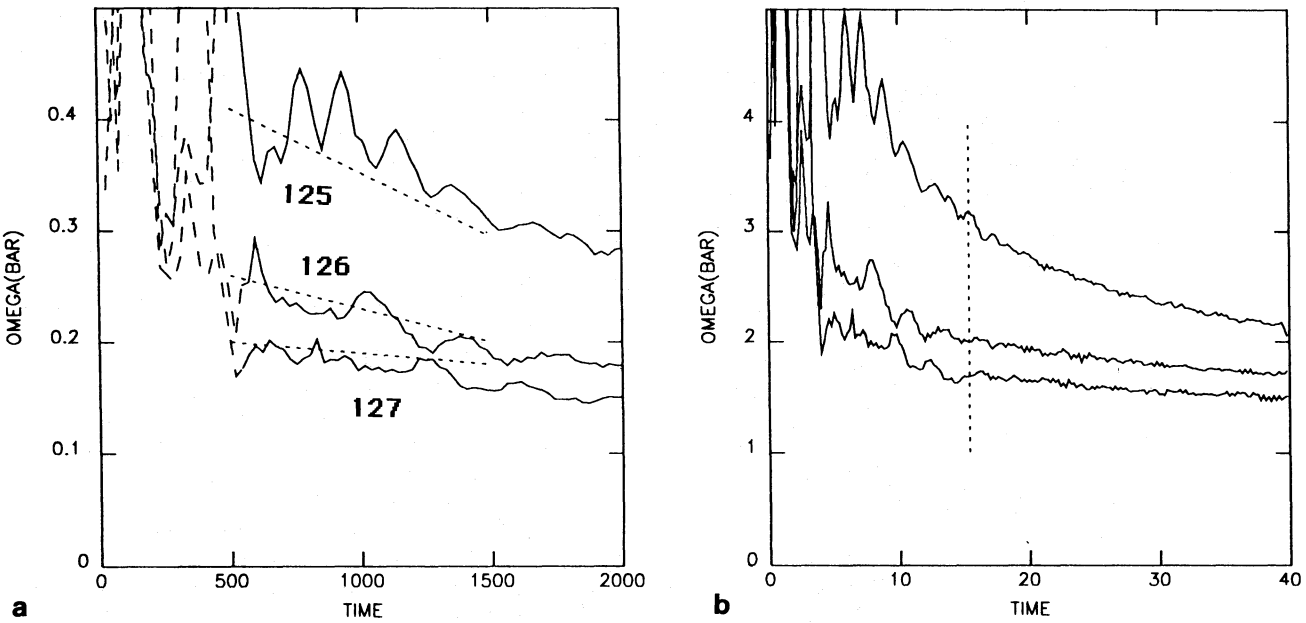

Fig. 2a and b. Comparison between the present simulation method and some of the simulations of Sellwood (1981), studying the bar formation in the case of single isolated galaxy with $M_{\rm disk}/M_{\rm tot} = 0.75$. The observed bar rotation rates (solid lines, calculated from particles residing inside $0.5\ R_{\rm disk}$) are compared for three models with variable degree of halo concentration. Equation (7) has been used for the disk with $a/R_{\rm disk} = 0.20$, while the halo parameter $b/R_{\rm disk}$ in Eq. (8) is 0.06, 0.12, and 0.20 (Sellwood's models 125, 126, and 127 respectively). Dashed lines are constructed from the "initial" and "final" rotation rates given by Sellwood. In **a** Sellwood's units are adopted, while in **b** the same simulations are shown in our time units, for a longer duration (vertical line in **b** indicates the time corresponding to $T = 2000$ in Sellwood's units). All the essential model parameters (initial velocity dispersion, softening-length, particle number, disk truncation radius, etc.) are similar to those used by Sellwood. Bar rotation rates were calculated by determining the directions of the principal axis of inertia after every 10 time steps (time step was 0.02 simulation units, corresponding to about 600 steps/orbit in the outer parts of the disk)

mass in the disk with respect to the inert halo. Large value of softening can also prevent bar formation, but its physical justification is questionable (see discussion by Sellwood 1981, 1986). Therefore, the value $\varepsilon = 0.06$, adopted by Sellwood (1981) is used throughout these experiments. Notice that here ε is a constant fraction of $R_{\rm disk}$ and does not depend on disk scale-length a. Since excessively large velocity dispersion does not only prevent bar instabilities but also suppresses the effects of tidal interactions, the disk velocity dispersion has been limited by choosing $Q_T = 1$ for the Toomre stability parameter. Several test runs were then carried out decreasing the $M_{\rm disk}/M_{\rm tot}$ ratio (here $M_{\rm disk}$ and $M_{\rm tot} = M_{\rm disk} + M_{\rm halo}$ denote the initial masses inside the truncation radius $R_{\rm disk}$) until essentially stable behaviour was found, except for transient spiral features. This was done separately for more concentrated models, with $a = b = 0.2$ and for less concentrated ones, $a = b = 0.5$. Since a equals b, the relative contributions of disk and halo are independent of distance and depend only on the mass ratio. In these and all the subsequent runs, $N = 20000$ particles have been simulated and the timestep has been 0.02 simulation units (fixed by setting $M_{\rm tot} = 1$, in which case circular orbit at unit distance requires about 2π time units). Simulation units can be scaled to physical units by assigning numerical values to $M_{\rm tot}$ and $R_{\rm disk}$. For example, by choosing $M_{\rm tot} = 2\ 10^{11}\ M_\odot$, $R_{\rm disk} =$ 20 kpc, simulation time unit corresponds to about 94 10^6 yr, and velocity unit to 208 km s^{-1}.

Figure 3 collects some of the results of these initial test runs: as can be seen, for $M_{\rm disk}/M_{\rm tot}$ close to unity, 0.75, the systems strongly deviate from axial symmetry in less than 10 simulation units, corresponding to about two rotation periods. After the rapid initial evolution, the shape of the bar remains essentially constant, although its rotation rate is gradually decreasing (see Fig. 3b and also Fig. 2). For $M_{\rm disk}/M_{\rm tot} \approx 0.5$, the onset of instability takes longer, but in agreement with the survey of Sellwood (1985), long-term stability seems to require $M_{\rm disk}/M_{\rm tot}$ to be less or of the order of 1/3. Therefore, this value has been chosen as the standard value in our perturbed runs, although a few cases with smaller $M_{\rm disk}$ are also studied. However, for $a = b = 0.5$ $M_{\rm disk}/M_{\rm tot}$ could be increased to about 0.4 and the disk remained practically stable for almost to the end of the simulation. The fact that larger self-gravitating mass leads to slower rotation rate probably follows from the strong initial expansion of the system when the bar starts to form. Also, the observed gradual decrease of rotation rate probably reflects the slow expansion of the system.

The four standard mass-models chosen for further studies are illustrated in Fig. 4. In these models $a = b$ varies from $0.2\ R_{\rm disk}$ to $0.5\ R_{\rm disk}$, while the ratio $M_{\rm disk}/M_{\rm tot} = 0.33$. As the degree of central condensation decreases the rotation curve of Model I, which is steeply rising near the center and mildly decreasing in outer disk, is gradually transformed into monotonically rising rotation curve of Model IV. Estimated relaxation times (Fig. 4, last panel) vary between 10 to 40 simulation units, which are of the same order as the lengths of the simulations (typically 50 time units, or about 8 rotations at the edge of the disk). Therefore, bars appearing with a very long formation time-scale are somewhat *susceptible* since they might manifest the effects of unsuppressed relaxation and be thus related to some secular instability as proposed by White (1988). This might be supported by the fact that for $M_{\rm disk}/M_{\rm tot} = 0.50$ and 0.40, bar formation takes longer with $a = b = 0.5$, having also longer relaxation time-scale. However, tests carried out with $N = 40000$ particles did not reveal any significant differences, so that the role of the relaxation remains unclear. The only noticeable difference was found in runs with

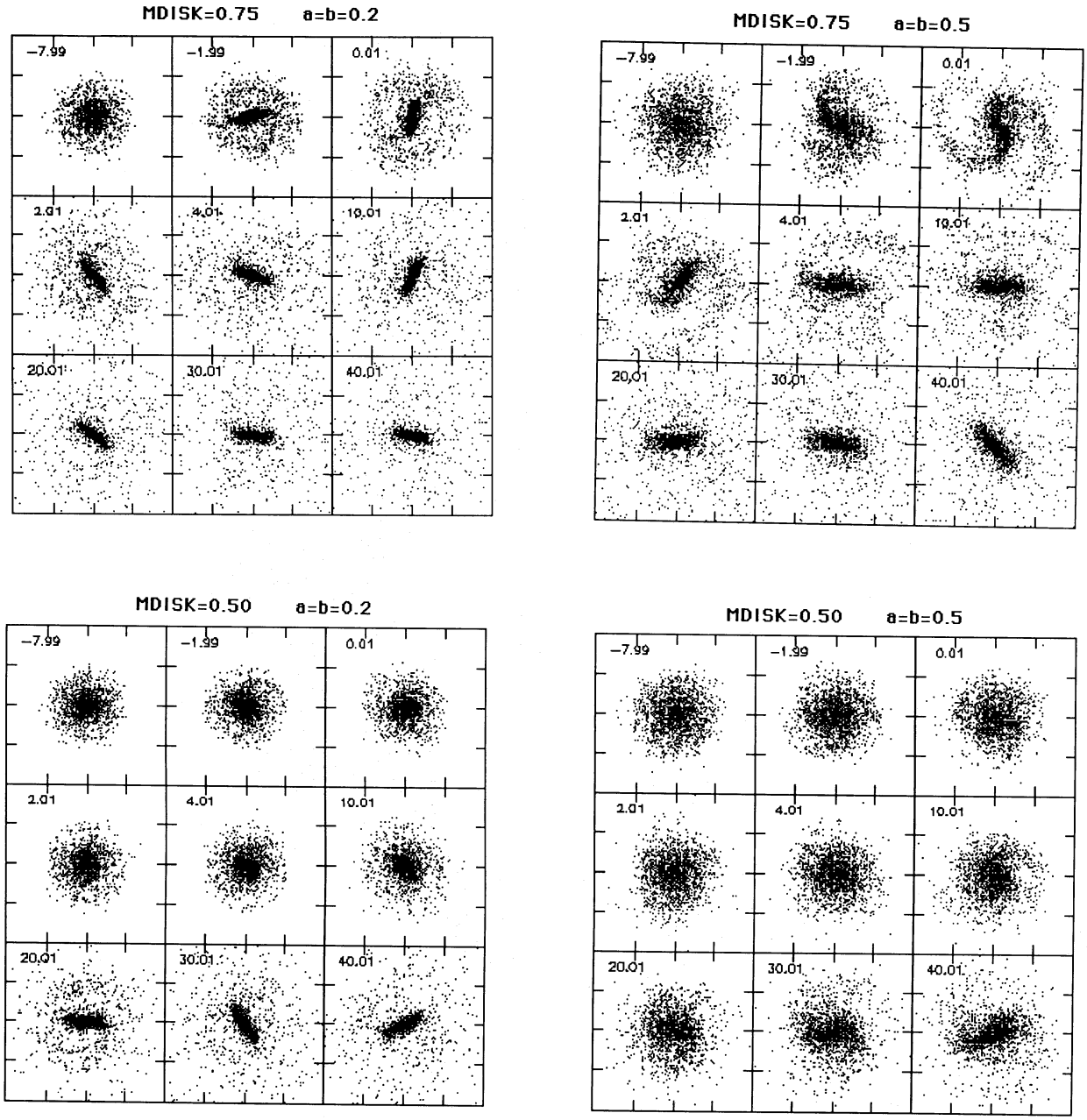

Fig. 3a. Examples of bar formation in isolated galaxy. Particle projections in runs with various combinations of M_{disk} and $a = b$ are shown. Numbers denote time in simulation units. More concentrated mass model leads to shorter bar in shorter timescale

$N = 10000$ and $N = 40000$ particles: in the former case random velocity dispersions increased in a slightly larger rate. However, since it seems evident that relaxation effects are negligible in the case of strong, rapidly forming bars, we will not consider this problem any further in the present context. Also, since tidal forces increase random velocity dispersion, initial relaxation times underestimate the real ones.

4.2. Tidal bar formation in stellar component

The strength of the tidal perturbation can be conveniently described with the Dahari parameter, $Q_D = (M_{\text{pert}}/M_{\text{tot}})/(R_{\text{min}}/R_{\text{disk}})^3$, estimating the direct tidal impulse. Figure 5 displays some examples of the time-evolution in simulations of Model IV, perturbed by direct parabolic encounter with various minimum separations, R_{min}, while adjusting M_{pert} so that Q_D stays constant. Here M_{pert} stands for the mass of the perturber, described with a point-mass (or, more accurately, with a Plummer sphere with scale radius of 0.06). Relatively large perturbation has been applied, namely $Q_D = 0.125$. For $R_{\text{min}} > 1$, stellar bar is induced in a very short time scale after the closest passage, in close agreement with the experiments of Noguchi (1987). Most importantly, as long as the minimum separation is above about 1.5 R_{disk}, the evolution stays essentially the same in spite of the huge mass difference in perturbing masses. Also, the final rotation rates of the bar are essentially similar, varying

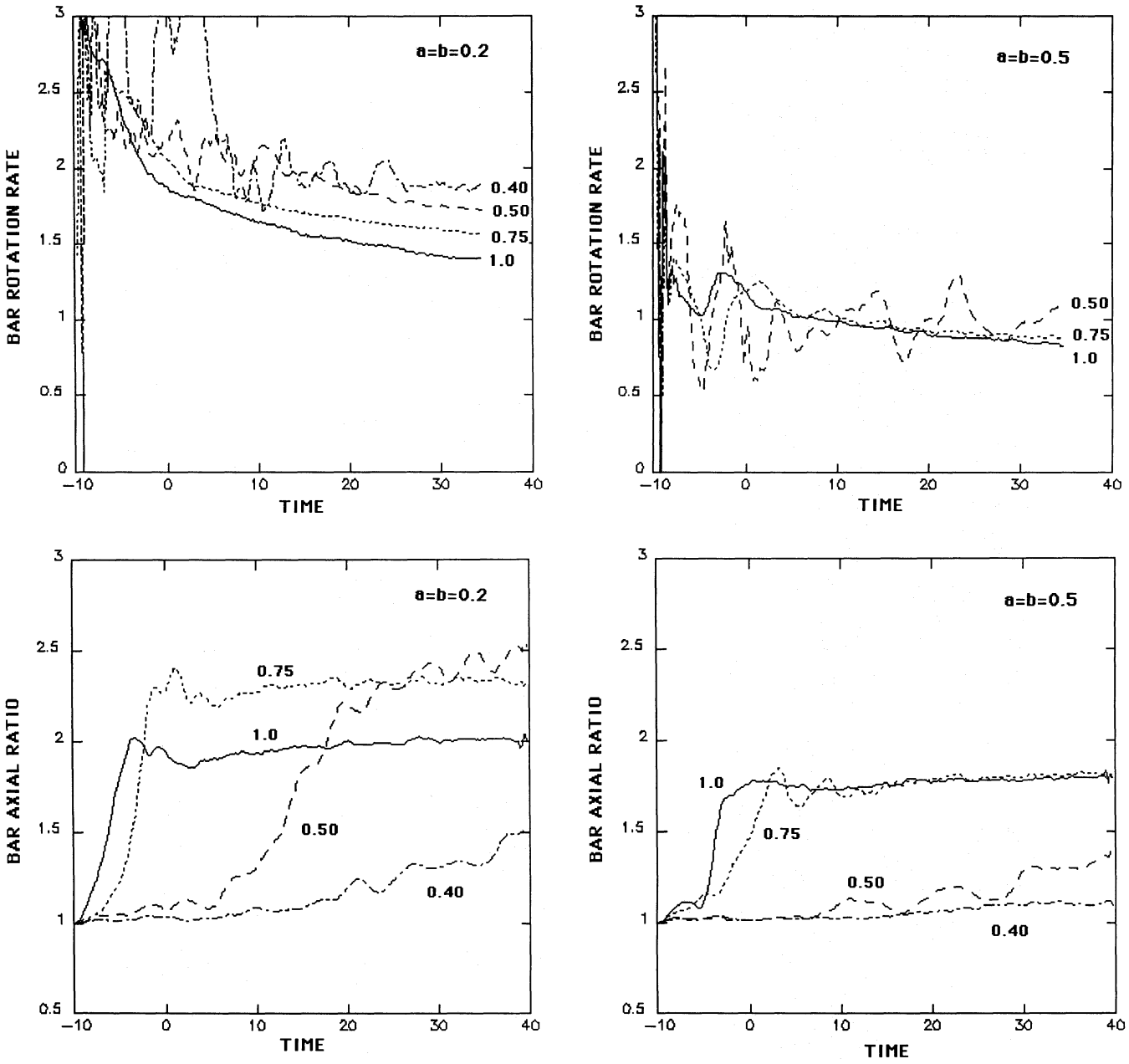

Fig. 3b. Evolution of bar rotation rates and axial ratios in simulations of isolated galaxies. Compared to Fig. 3a, two additional $M_{\rm disk}$ values are studied. For clarity, in the case $a = b = 0.5$, $M_{\rm disk} = 0.4$, the rotation rate for the forming weakly elongated feature is not plotted

between 0.55 and 0.65 for $R_{\rm min} > 1.5$. However, close encounters with small perturbers do not induce as clear a response as massive distant ones. In any case, as long as we exclude penetrating passages, Q_D itself seems sufficient to describe the perturbation, and various combinations of $R_{\rm min}$ and $M_{\rm pert}$ need not be considered separately. A few additional runs were also performed with hyperbolic passages with $R_{\rm min} = 2$, but they led to essentially same behaviour. For more concentrated models I, II, and III, the dependence on $R_{\rm min}$ should be even weaker.

The dependence of tidally triggered bar formation on the shape of the rotation curve is illustrated in Figs. 6 and 7. The former figure displays the effects of strong perturbation on all four models, while the latter compares in detail the bars formed in the extreme Models I and IV. In each case the point-mass perturber moves in a direct parabolic orbit. According to Fig. 6, as the degree of central condensation is increased (Models II and I) the formation of bar takes longer and results in a rounder and more rapidly rotating feature. In fact, in the case of Model I, based on the projections only (Fig. 6a) it would be tempting to describe the result as a tightly wound spiral, although plots of the rotation rate (Fig. 6b) show that a rigidly rotating bar is indeed formed. However, much larger perturbation is needed in Model I as compared to Model IV (Fig. 7) in order to produce a distinct bar. In the former case $Q_D = 0.125$ ($M_{\rm pert} = 1$, $R_{\rm min} = 2$) is just about the minimum required for the bar to form, at least during the duration of the simulation. On the other hand, in Model IV

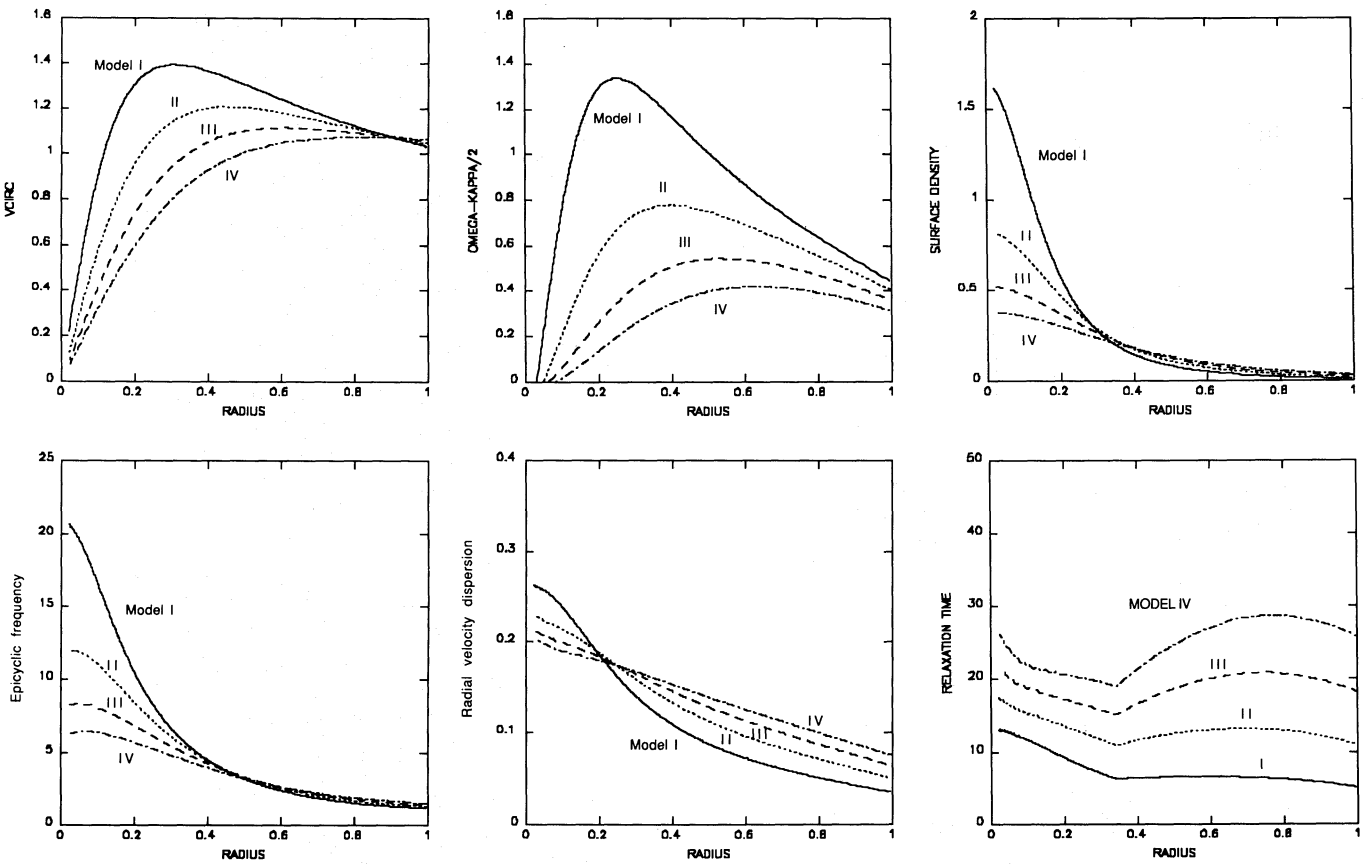

Fig. 4. Models used in the simulations. Eqs. (7) and (8) are used for the disk and halo, with $a = b = 0.2$, 0.3, 0.4, and 0.5 (Models I, II, III and IV, respectively). The ratio $M_{\rm disk}/M_{\rm tot}$ is fixed to 0.33, where $M_{\rm tot}$ is the total mass of the of the disk + halo inside the disk truncation radius $R_{\rm disk} = 1$. The value $\varepsilon = 0.06\, R_{\rm disk}$ has been adopted for the softening length, while the Toomre parameter $Q_{\rm T} = 1$. The relaxation time estimates are based on White's (1988) Eq. (4), and take into account both the explicit softening (dominates in the inner regions) and that due to finite grid resolution (outer disk)

$M_{\rm pert} = 0.25$ ($Q_D = 0.03125$) still leads to a bar-like elongation in time-scales shorter than the relaxation time.

According to Fig. 6b, there is a smooth transition in the bar characteristics as a function of parameter $a = b$: as the model is made more concentrated a shorter and rounder but more rapidly rotating feature is obtained. Also, it is important to note that although there is a minimum amount of perturbation required for the triggering of bar, once the bar is formed its rotation rate seems to be only slightly dependent on the perturbation, being essentially determined by the initial mass model (Fig. 7b). Indeed, the rotation rates of tidally induced bars for Models I, and IV, $\omega_{\rm bar} \approx 1.7$ and 0.6, respectively, are fairly similar to those implied by Fig. 3 for corresponding unstable isolated models. On the other hand, the time-scale and final strength of bar depends on the perturbation level: in the case of strong perturbation, the direct tidal distortion is almost directly transformed into permanent bar, while for weaker perturbation the bar formation can be delayed by several time units (compare curves for Model IV in Fig. 7b). For strong, thin bars the final rotation rate is slightly lower than for weaker features, probably simply reflecting their larger radial extent.

All the above experiments refer to relatively high disk mass, $M_{\rm disk}/M_{\rm tot} = 1/3$. One might assume that decreasing disk mass would make bar formation more difficult, since this must relay on the self-gravitation of the perturbed disk. Indeed, when $M_{\rm disk}/M_{\rm tot}$ was reduced to 0.2 in Model I, perturbation with $M_{\rm pert} = 1$, $R_{\rm min} = 2$ could not produce any long lasting bar: initial tidal distortion disappeared into tightly wound spiral, the system retaining its round overall shape. Run with $M_{\rm pert} = 2$ gave similar result. However, in the case of Model IV, even $M_{\rm disk}/M_{\rm tot} = 0.1$ resulted in a permanent bar shaped feature with similar perturbation, although rounder and weaker than with the standard disk-halo mass-ratio. This explains why Noguchi (1987) obtained bars although the maximum amount of active self-gravitating material in his experiments was only 0.20: his rotation curves resemble mostly our Model IV.

Some experiments were performed also with retrograde perturbers. However, even with $R_{\rm min} = 2$, $M_{\rm pert} = 16$ ($Q_D = 2$), no bar-like features were obtained in any of the studied models (with standard ratio $M_{\rm disk}/M_{\rm tot} = 0.33$), although rather strong spiral features were observed. In contrast to results of Thomasson et al. (1989), typical long-lasting tidal spirals were found to be trailing, just as in the case of direct perturbation, whereas some weak leading spirals were observed but only just after closest passage. On the other hand, Thomasson et al. (1989) postulate that with strong retrograde perturbation ($Q_D > 1$) and massive halo ($M_{\rm halo}/M_{\rm tot} > 0.5$) leading spirals should dominate. Since both these conditions were fulfilled in the above mentioned experiments, the discrepancy must follow from the different mass-model studied, Kuzmin disk instead of Mestel disk used by Thomasson et al. Regarding bar formation, it is of interest to note that in Model IV, increasing the $M_{\rm disk}/M_{\rm tot}$ from 0.33 to 0.40 lead to a

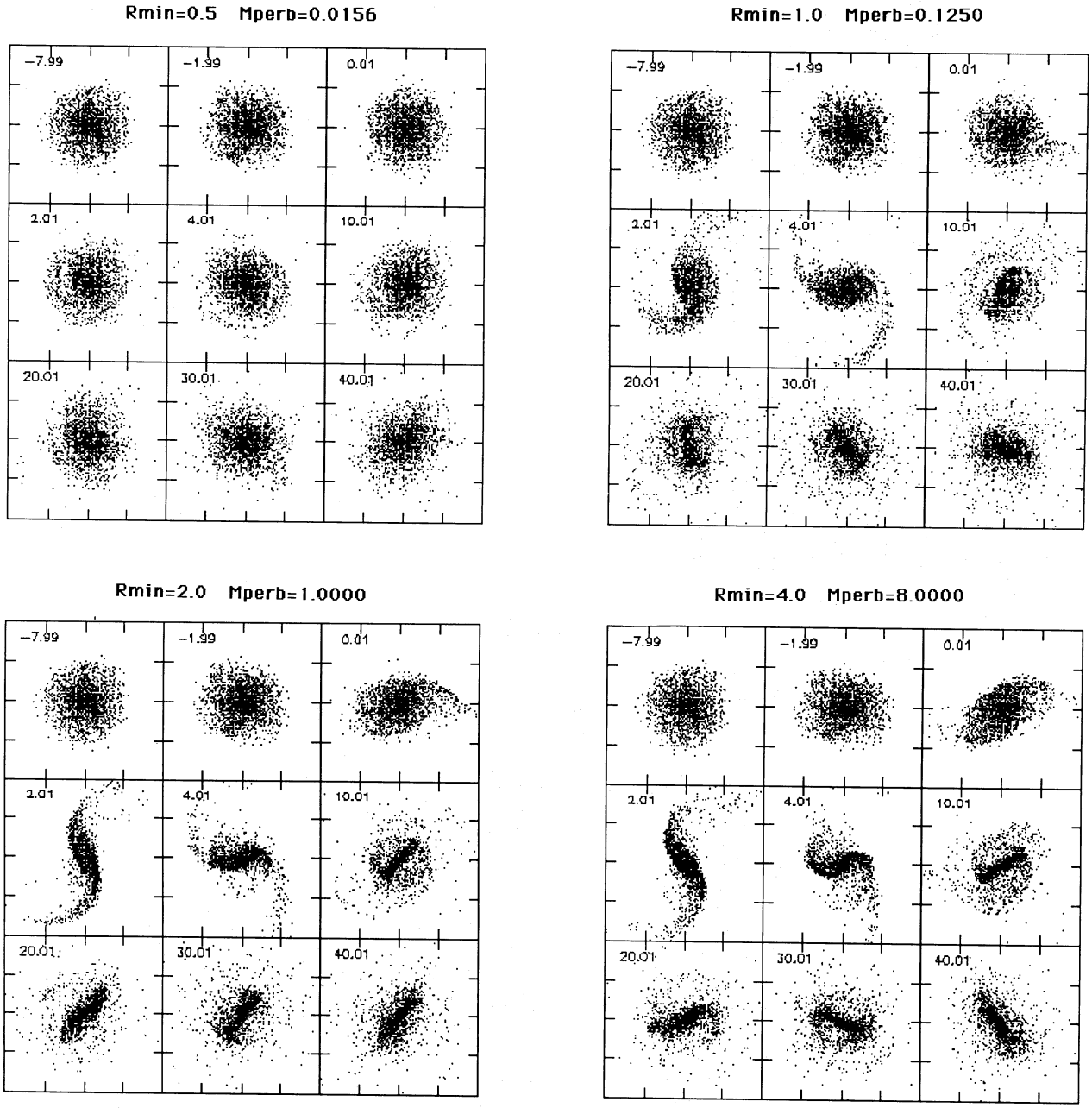

Fig. 5. Evolution of the Model IV in simulations with direct parabolic point-mass passage, with various minimum distances. Constant level of perturbation, $Q_D = 0.125$, is applied. Simulations started at $T = -10$ and the closest passage occurred at $T \approx 0$. The evolution of particle distributions is plotted at various times (2000 particles are shown, out of total number of 20000 particles)

clear bar also in the case of retrograde passage ($R_{min} = 2$, $M_{pert} = 1$), although the model was practically stable without perturbation. Therefore, even retrograde encounters can significantly strengthen the tendency for bar formation in the case of initially mildly unstable system.

5. Evolution of gas component

Results of some preliminary runs with gas-component included are displayed in Figs. 8 and 9. In these runs the gas component was described with 2000 non-selfgravitating particles, with radius of 0.001, initially distributed in a homogeneous disk extending to R_{disk}. The coefficient of restitution was fixed to $k = 0.5$ and the gas time step was 0.005, 4 times smaller than for stellar particles. Without any perturbation the gas distribution and cloud-cloud collision rate remains essentially constant during the length of the simulation. On the other hand, in the case of perturbation the collision rate increases, and the formation of stellar bar can significantly alter the gas distribution.

Figure 8 shows the time evolution of the projection of gas particles in runs with the standard models I–IV (direct parabolic passage with $M_{pert} = 1$, $R_{min} = 2$), corresponding to Fig. 6 for stellar population. With Models I and II the gas particles become

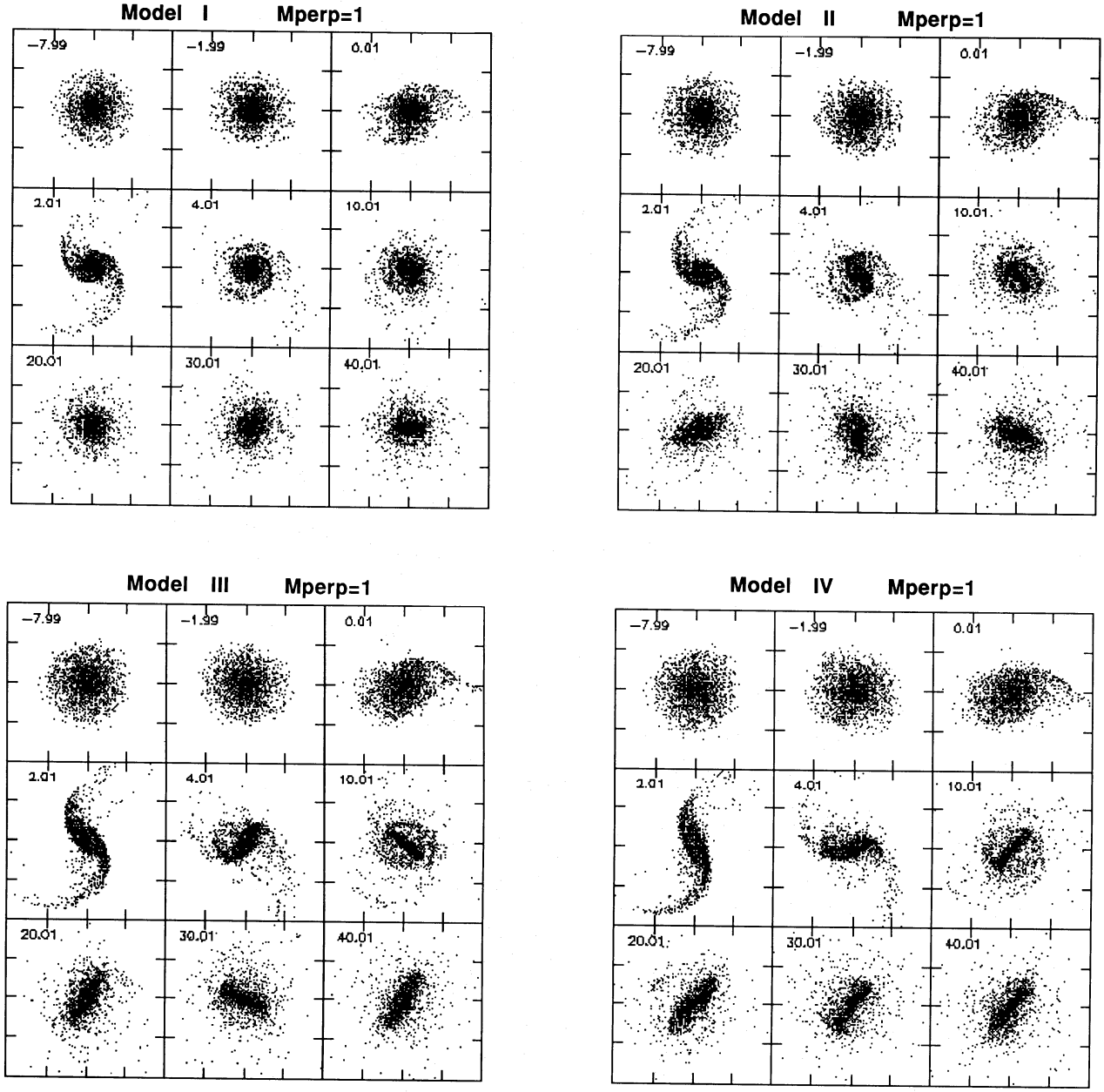

Fig. 6a. Influence of rotation curve on the bar formation. Models I–IV were perturbed by a point-mass perturber ($M_{\text{pert}} = 1$) in a direct parabolic orbit with minimum distance of two disk radii ($Q_{\text{D}} = 0.125$). The evolution of particle distributions is plotted at various times

gradually concentrated into an oval-shaped region, aligned with the stellar bar, whereas in Models III and IV, strong infall into nuclear regions occurs. This is somewhat hard to appreciate in the low resolution frames of Fig. 8, where for example in the case of Model IV most of the particles end up in practically one point. In fact, in the runs with Models III and IV the central regions become so densily populated that the collision frequency increases almost asymptotically into infinity (see Fig. 9 for the total number of impacts): this is the reason why run with Model IV could not be followed longer than 30 time units. For Model I, larger perturbations were also studied but they also lead to a ring-shaped concentration, although somewhat larger fraction of the particles ended up at nuclear regions. The formation of rings or rather, oval-shaped concentrations is probably due to trapping of gas into the inner Lindblad resonances. According to Fig. 4, the bar rotation rates are in every case higher than the maximum of $\omega - \kappa/2$ derived from the initial distribution, implying that no ILR should be present. However, even a slight increase in the central concentration can rise the maximum of $\omega - \kappa/2$ just enough to produce ILR. This phenomenon will be studied more carefully in future.

As shown by the right panel in Fig. 9, for Model IV even rather small perturbations can lead to a great increase of collision rate, due to flow of gas particles into the nuclear regions. Indeed, in agreement with Noguchi (1988), this is certainly not due to direct perturbation but happens only after stellar bar is formed, as can be

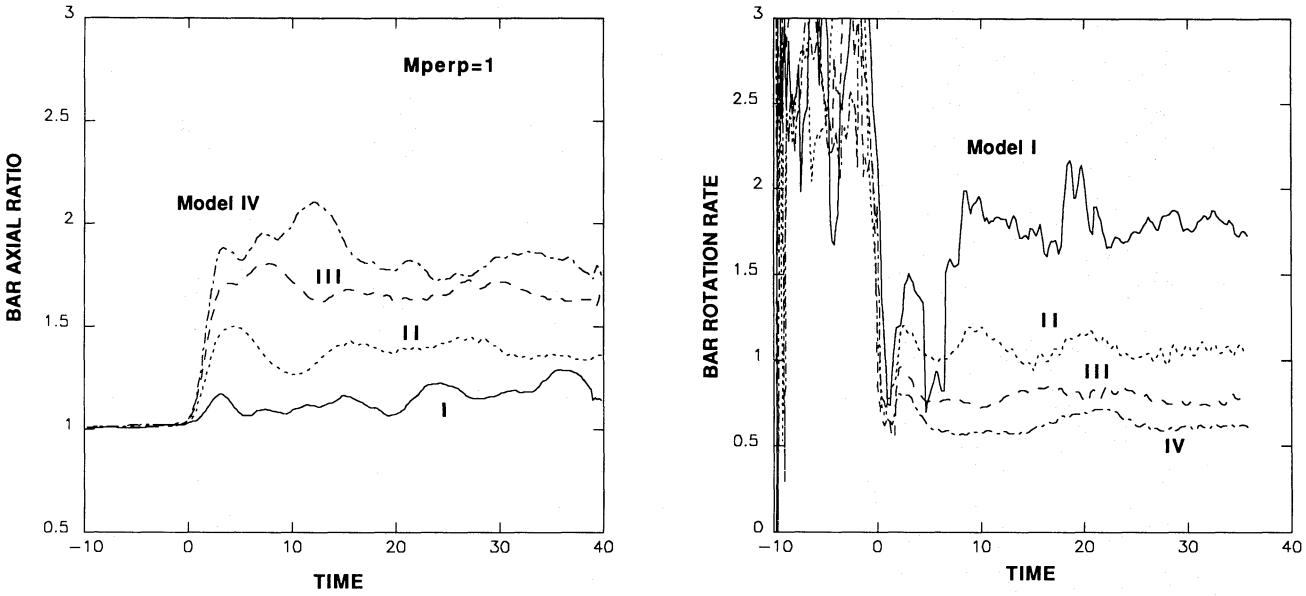

Fig. 6b. The evolution of bar rotation rates and bar axial ratios in simulations of Fig. 6a

clearly seen from the time delay between closest passage and the increase of collision rate. No corresponding strong concentration or infall was observed in the stellar population, in contrast with the results of Byrd et al. (1987). This might follow from the fact that Byrd et al. had a different mass-model, but also on their defination of infall: they counted the total number of particles which had crossed the central grid-hole at all times, without paying attention to the actual distribution of particles at the nuclear regions (see the discussion in Noguchi, 1988). However, it seems rather certain that only for the gas component, losing energy in dissipative processes, can there be any large-scale infall.

6. Two star + gas disks

As a final example of the potential applications of the new code, we describe a few examples of runs performed with more realistic encounters of two disk systems (Figs. 10 and 11). The primary galaxy had a Model IV mass distribution with $M_{\text{disk}}/M_{\text{tot}} = 0.33$, and radius $R_1 = 1$ and total mass $M_1 = 1$. The other system was described with Model I distribution, and had $R_2 = 0.5\,R_1$ and $M_2 = 0.5\,M_1$. The softening length for the smaller galaxy was one-half (0.03) of its value for the larger galaxy. Parabolic encounter with $R_{\min} = R_1 + R_2$ was studied. Gas component was described with a uniform surface density distribution, by 4000 non-selfgravitating particles in disk 1 and 1000 particles in disk 2, so that the gas surface density was the same in both systems. Coefficient of restitution was 0.5 and the radius assigned to gas particles 0.0001. In the case of two non-identical systems there are four different combinations of orbital geometry and internal rotation: we have studied the two cases where the passage is direct with respect to the rotation of the primary system, while from the viewpoint of secondary it is either direct or retrograde. These will be denoted as direct-direct and direct-retrograde encounter, respectively (see first frame of Fig. 11).

The runs described in the previous Sections can be used to estimate the behaviour in the direct-direct run. For the primary, $Q_D = 0.148$, which combined with Model IV mass distribution leads (see Fig. 7) into a strong bar immediately after the closest passage and rapid infall of gas towards nuclear regions (see Fig. 8). On the other hand, for the secondary Q_D is smaller, 0.074, which combined with the Model I mass-distribution should lead only to a very weak stellar bar and a mild ring-shaped gas concentration. This indeed happens: the run had to be terminated at about 17 time units after closest passage, due to excessively high collision rate in the nuclear regions of primary galaxy. At the same time, the ring feature in the secondary had just started to become evident (see last panel in Fig. 10). There had been a rather large transfer of material from the primary to the secondary, but it had not significantly altered the evolution of its original gas population. This follows from the gentle manner in which the mass transfer occurs: relative velocity of the systems tends to cancel the differences following from opposite rotations in the disk edges adjacent to each other.

The change of geometry into direct-retrograde passing did not affect the evolution of stellar populations in any significant manner: the only difference was the expected absence of tidal bridge originating from the secondary. Also, the outlook of the large scale tidal features in gas, determined by the larger system, are essentially similar (Fig. 10 upper panel). On the other hand, evolution of gas population in the secondary was dramatically different (middle panel in Fig. 10 and Fig. 11). In the case of direct-retrograde encounter the tidal gas bridge from the primary hits the secondary disk with practically full relative orbital velocity of the systems. Resulting high impact frequency leads to a very strong dissipation and almost immediate infall into nucleus when gas loses its rotational kinetic energy and angular momentum. Consequently, the run had to be terminated at only a few time units after closest passage, due to the excessive impact frequency in the nuclear region of the secondary. Notice the large amount of gas originating from the primary which ends up in the nuclear regions of the secondary (middle panel of Fig. 10). Notice however, that due to planar geometry the collision frequency is probably greatly exaggerated as compared to any realistic 3-D situation.

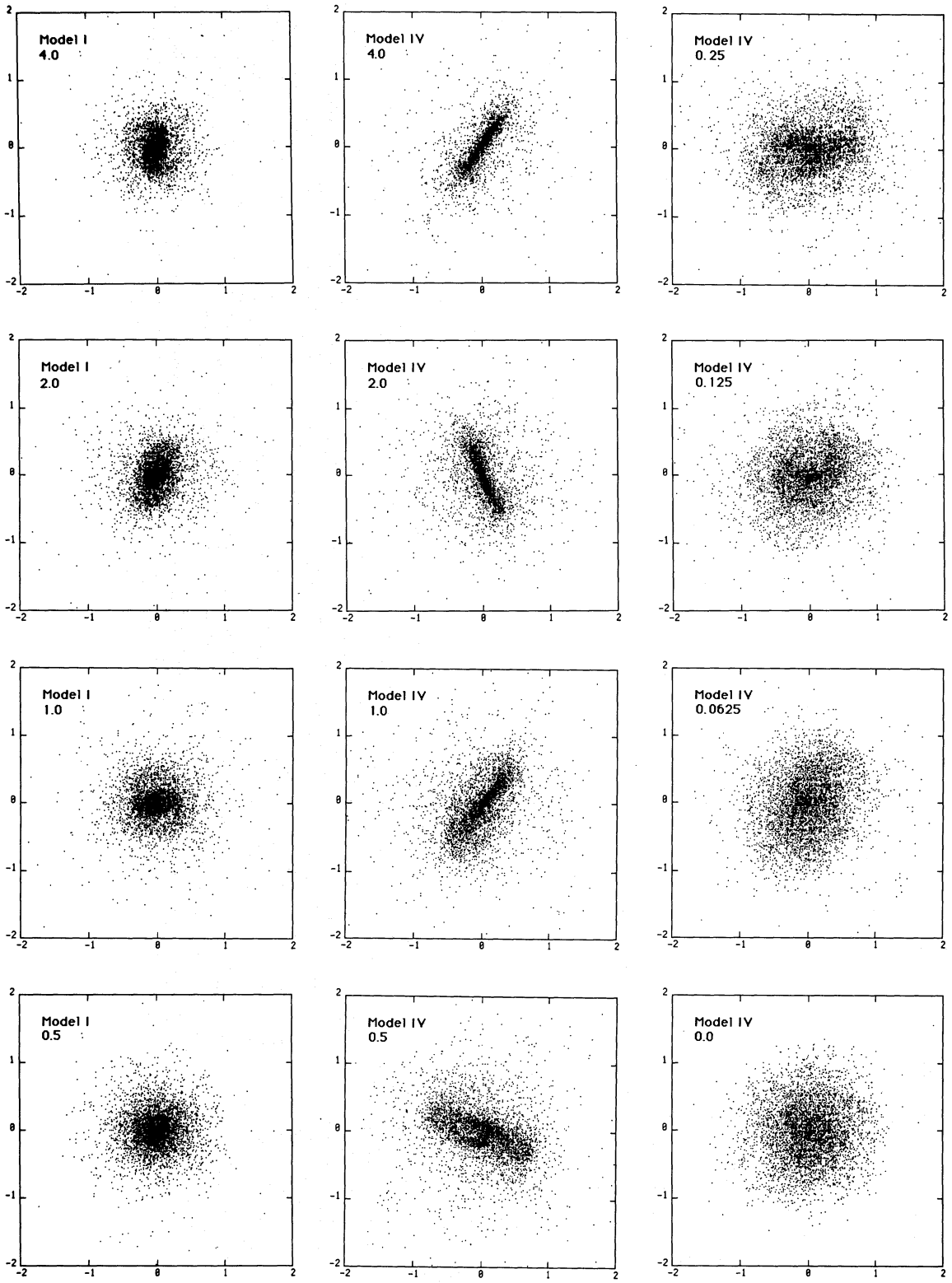

Fig. 7a. Response of the stellar population with decreasing amount of perturbation in Models I (left panel, $M_{\text{pert}} = 4.0 - 0.5$) and IV (middle and right panels, $M_{\text{pert}} = 4.0 - 0.0625$). Snapshots of the particle distributions at time $T = 40$ are shown for simulations where Models I and IV were perturbed by a point-mass passing in direct parabolic orbit with minimum distance of two disk radii. For comparison, the case with no perturbation is also shown for Model IV

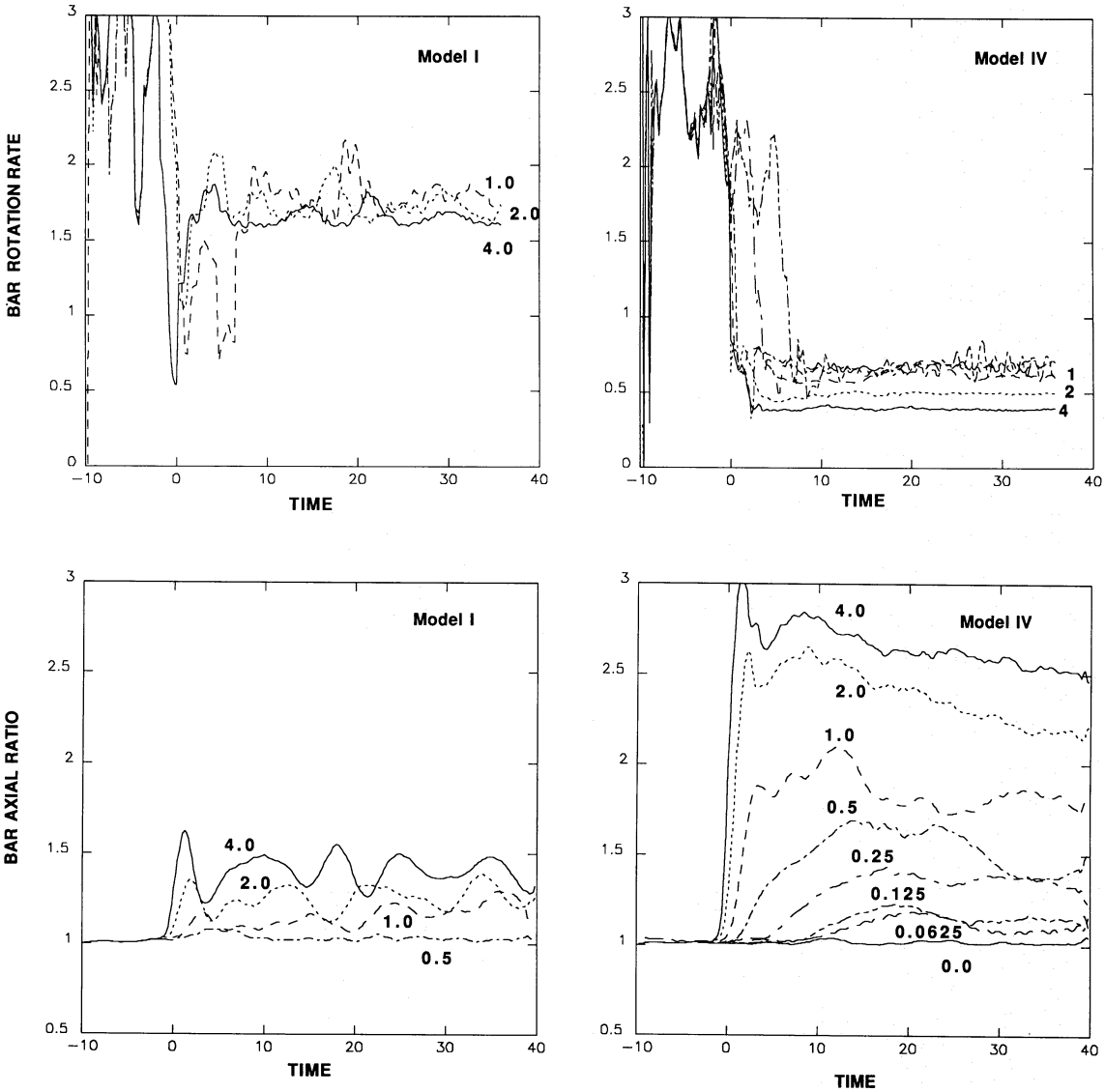

Fig. 7b. The evolution of bar rotation rates and bar axial ratios in simulations of Fig. 6a, shown separately for Models I and IV. For clarity, bar rotation rates are shown only for cases where clear bar was formed (for Model I, with $M_{\text{pert}} \geqq 1.0$, and for Model IV, with $M_{\text{pert}} \geqq 0.25$)

Clearly, the method used for collisional calculations must be modified in future studies, since it is not practical to follow every impact once the density gets too high. One possibility would be to let the code ignore some impacts, but this has to be done with extreme care. Especially, just in the case of gas streaming from one system to another, the present method with accurate calculation of impacts is probably the most reliable one, since it makes it possible to follow the evolution also with large relative velocities, something which is much harder to do when collisional "bins" are used. In fact, an additional test was performed for the above direct-retrograde case, in which the limiting initial distance for the search of colliding pairs during step was not allowed to exceed 4 particle diameters. Combined with the step size of 0.005 this means that many of the impacts where the relative velocity was above $8\ 10^{-4}/5\ 10^{-3} = 0.16$ were missed, therefore mimicking the less accurate collisional methods. This does not significantly alter the initial evolution of gas when the collisions are determined by the random velocity dispersion inside a single system. However, in the region where the gas from different systems overlaps, the behaviour is very different, the gas streams largely penetrating each other. This led to a clear delay in the infall as compared to the more accurate method.

7. Conclusions

A new 2-dimensional code for studies of planar encounters of two disk+halo systems has been introduced. In addition to stellar disks, gaseous components are included, as well as a simple model for star formation. In future, the code will be applied to detailed studies of star formation activity in interacting systems. In the present paper some preliminary applications were presented, mainly extending Noguchi's (1987) studies of tidally triggered bars, and verifying them with an independent computational method. Examples showing the potential possibilities of the code

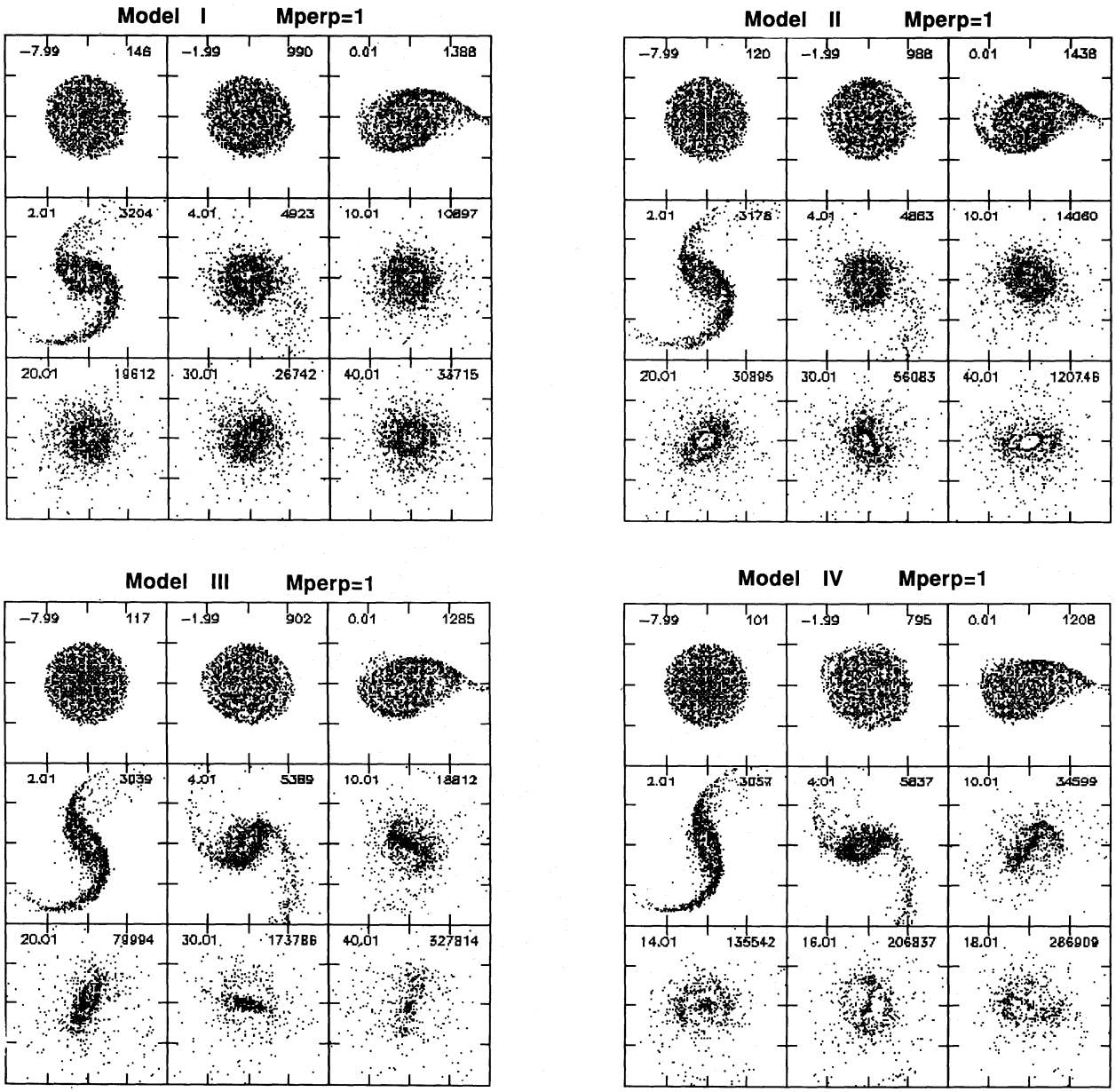

Fig. 8. Evolution of gas-particles in four simulations with Models I, II, III, and IV. In each experiment, direct parabolic encounter with $M_{\text{pert}} = 1$, $R_{\min} = 2$, was studied, corresponding to Fig. 6 for the stellar component. Total number of collisions is shown in each frame. For Models I, II, and III, the simulation extended to $T = 40$, while for Model IV, the simulation was terminated at $T = 18$, due to excessive amount of impacts (see text). Although not clearly visible in the plot, for this case almost all gas particles became concentrated in the nuclear area

on studies of gas behaviour and gas transfer between systems were also given.

The main results concerning tidally triggered stellar bars can be summarized as follows:

1) The formation of stellar bars was shown to depend on the simultaneous effects of the rotation curve, disk-halo mass ratio, and the strength and geometry of the perturbation. However, a single parameter, Q_D, describing the direct tidal impulse, seems to be sufficient to describe the strength of the direct perturbation, if penetrating encounters are excluded.

2) For more centrally concentrated mass-models, stronger levels of perturbation are needed in order to obtain bars: for Model I, Q_D must be larger than about 0.125, while for model IV, $Q_D > 0.0325$ is sufficient (for standard ratio $M_{\text{disk}}/M_{\text{tot}} = 1/3$). Importance of disk-halo mass ratio depends also on rotation curve: for Model I smaller active disk mass prevents bar formation, while for Model IV it has less significance.

3) Pattern speed of the bar, once triggered, is determined mainly by the rotation curve, and is not much affected by the strength of the perturbation, being fairly similar to that obtained with unstable disk-halo mass ratios for corresponding isolated models.

4) Timescale of the bar formation gets longer with smaller perturbation, and the resulting bar is typically weaker and

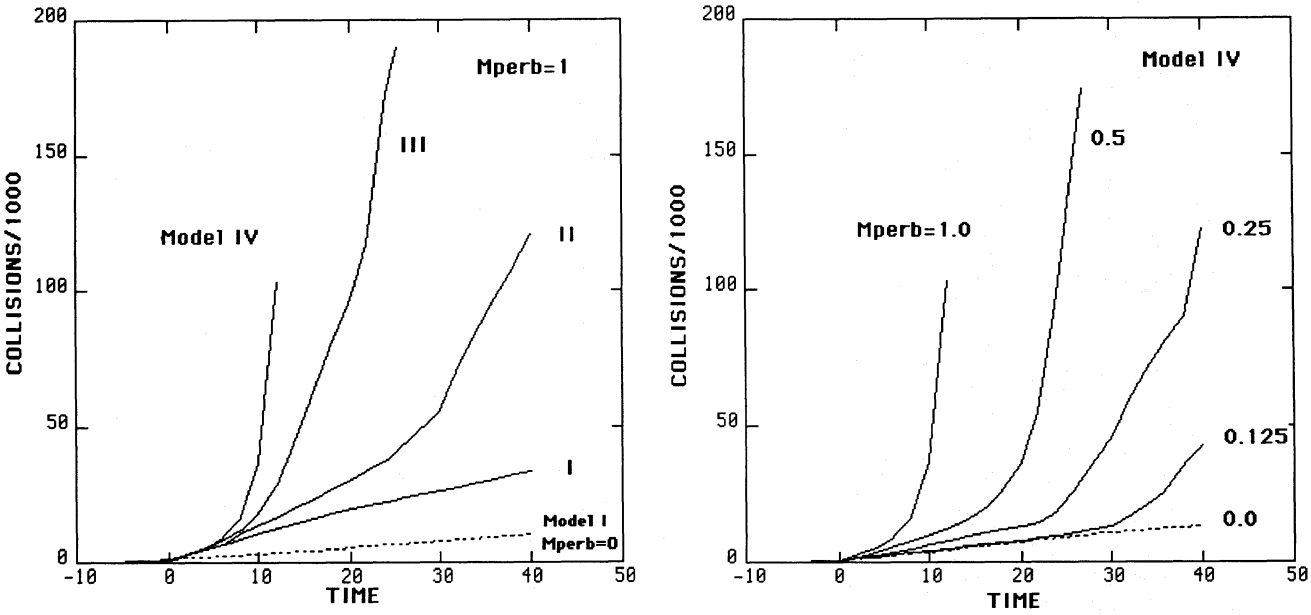

Fig. 9. The evolution of total number of cloud-cloud collisions in simulations with various rotation curve models (left-hand side plots correspond to simulations of Fig. 8), and with Model IV with decreasing degrees of perturbation (right-hand side plots)

rounder. In the case of strong perturbation, the tidal distortion is directly transformed into bar whereas for small perturbation, bar forms only slowly after closest passage. Extremely long formation timescales are, however, susceptible due to uncertain effects of 2-body relaxation.

5) Retrograde encounters are not capable of triggering bar formation in initially stable systems. However, they can significantly speed up the growth of bar instability in marginally unstable cases.

Tidally induced stellar bars were shown to be able to induce infall of gas into nuclear regions, as already shown by Noguchi (1987). However, for centrally concentrated models formation of gas rings was found to be the more likely outcome. Also, rather small perturbations could induce infall, but with longer delays after closest passage. No corresponding infall was observed in the stellar component.

Just one example of two disk runs was presented. It showed that the results of point-mass perturbers are applicable unless the gas transfer between systems become important. An important difference was found in the case of direct-direct and direct-retrograde encounters, the latter leading to stronger activity in the gas component of the secondary system. The example is rather extreme, since the plane restricted geometry leads to unrealistically strong exchange of material, but nevertheless suggests that factors related to internal kinematics can in principle affect the observed activity in complicated ways. It also demonstrated the importance of accurate collisional calculations. In future more systematic surveys of two disk encounters will be reported. Also, extensions to 3 dimensions will be investigated.

Acknowledgements. The author is grateful to the referee, Dr. J. Sellwood for his most useful comments and suggestions. The support from Wihuri Foundation and Finnish Cultural Foundation is also acknowledged. The simulations were performed with the Cray X-MP of the Finnish Ministry of Education.

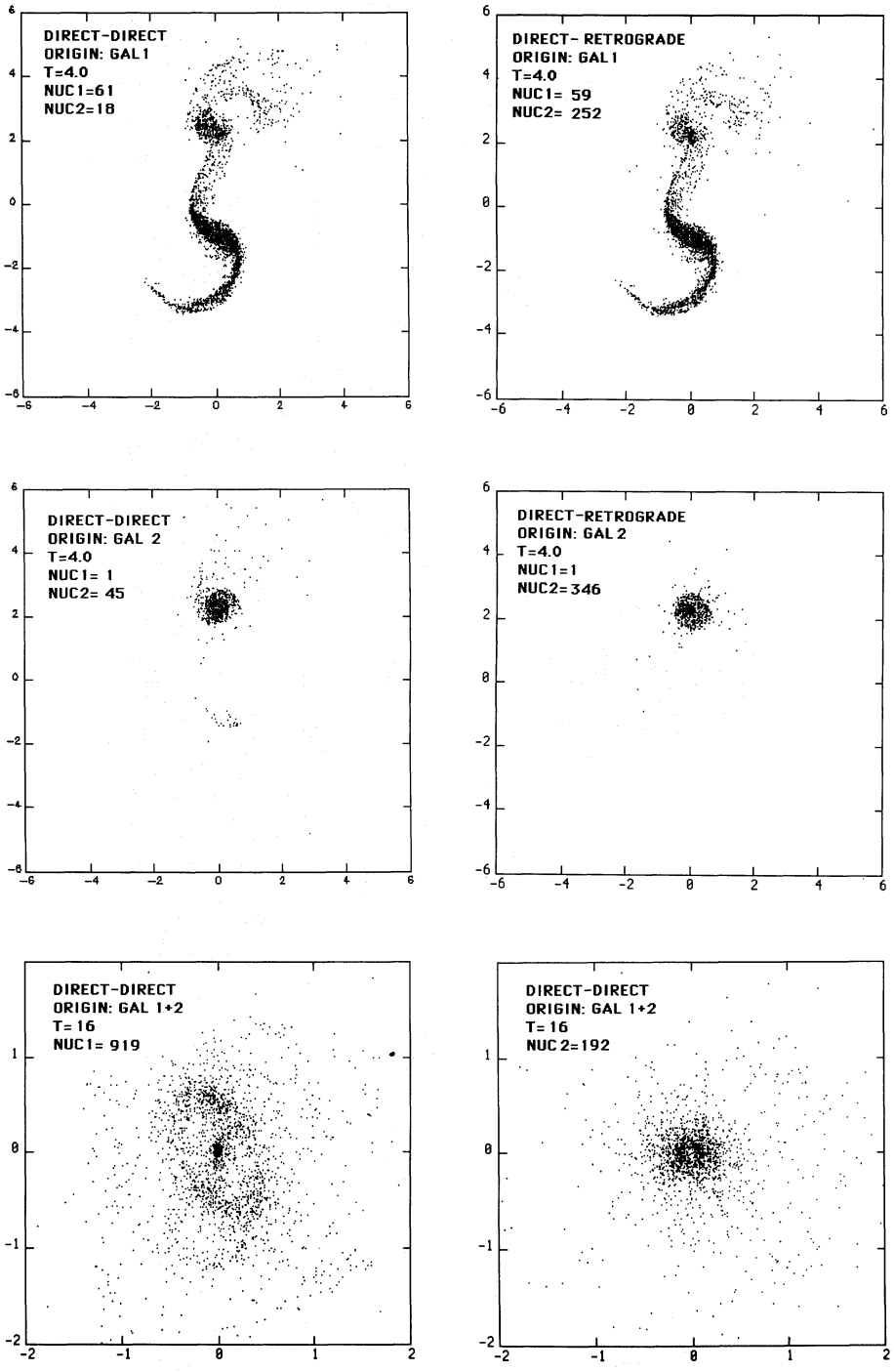

Fig. 10. Example of 2-disk simulation described in the text. Upper and middle panels show the gas distributions for direct-direct and direct-retrograde runs at time $T=4$. Gas particles originating from different systems are shown separately: NUC1 and NUC2 denote the numbers of gas particles which have fallen inside the central 0.1 R_{disk}-regions in the primary and secondary, respectively (originally, NUC1 $\approx$ NUC2 ≈ 40). The direct-retrograde run was terminated at this point. The last panel shows the gas particle distributions close to the end of the direct-direct run, at $T=16$. In the primary, infall has occurred, while in the secondary a ring is starting to emerge

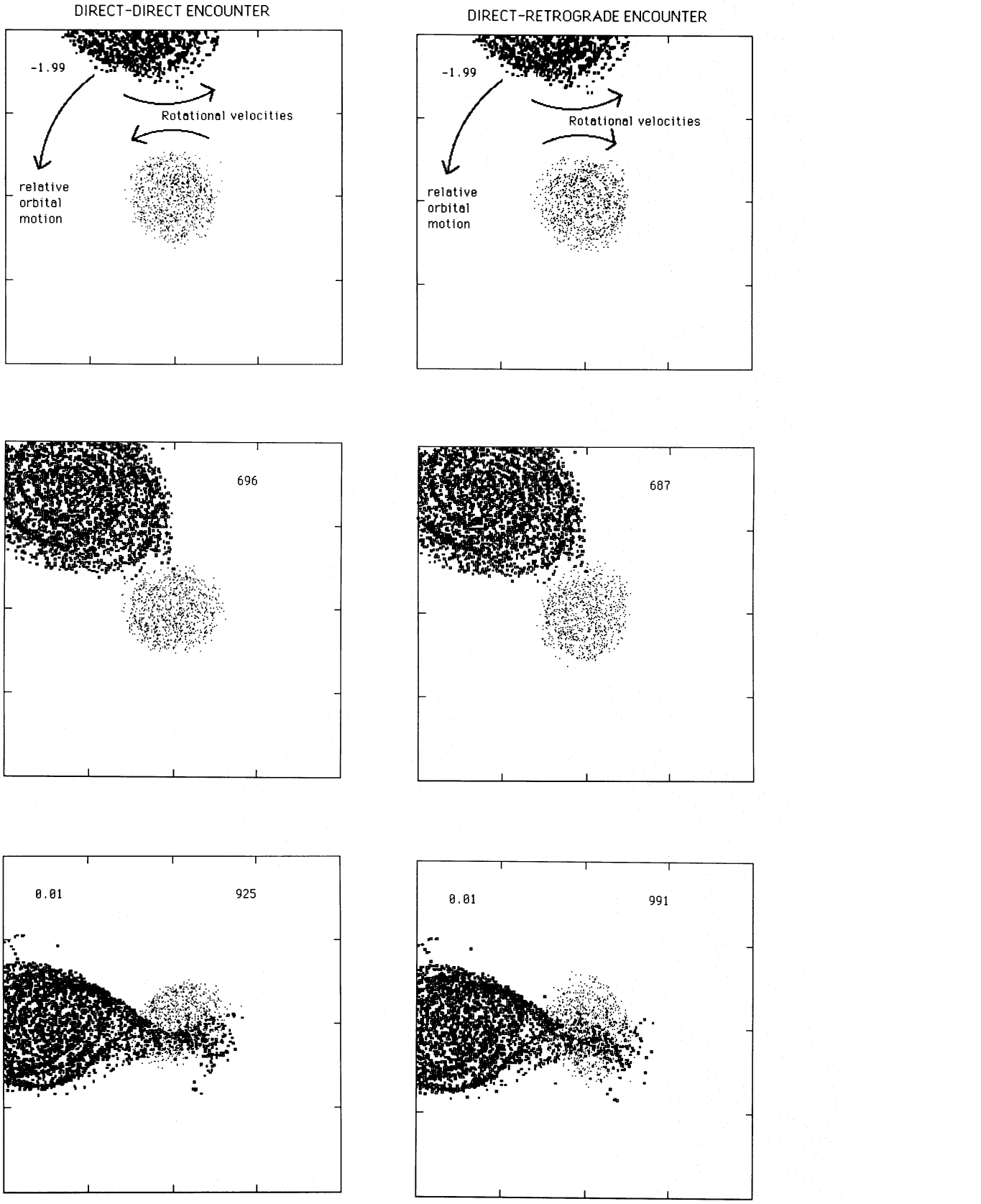

Fig. 11. Details of the direct-direct and direct-retrograde runs. Distribution of the gas in the 4 simulation unit wide region around the secondary galaxy is shown, different symbols denoting particles from different systems. Notice the strong, immediate infall into secondary in the direct-retrograde case (right-hand side frames). The numbers in the frames refer to the time of the projection and the total number of impacts

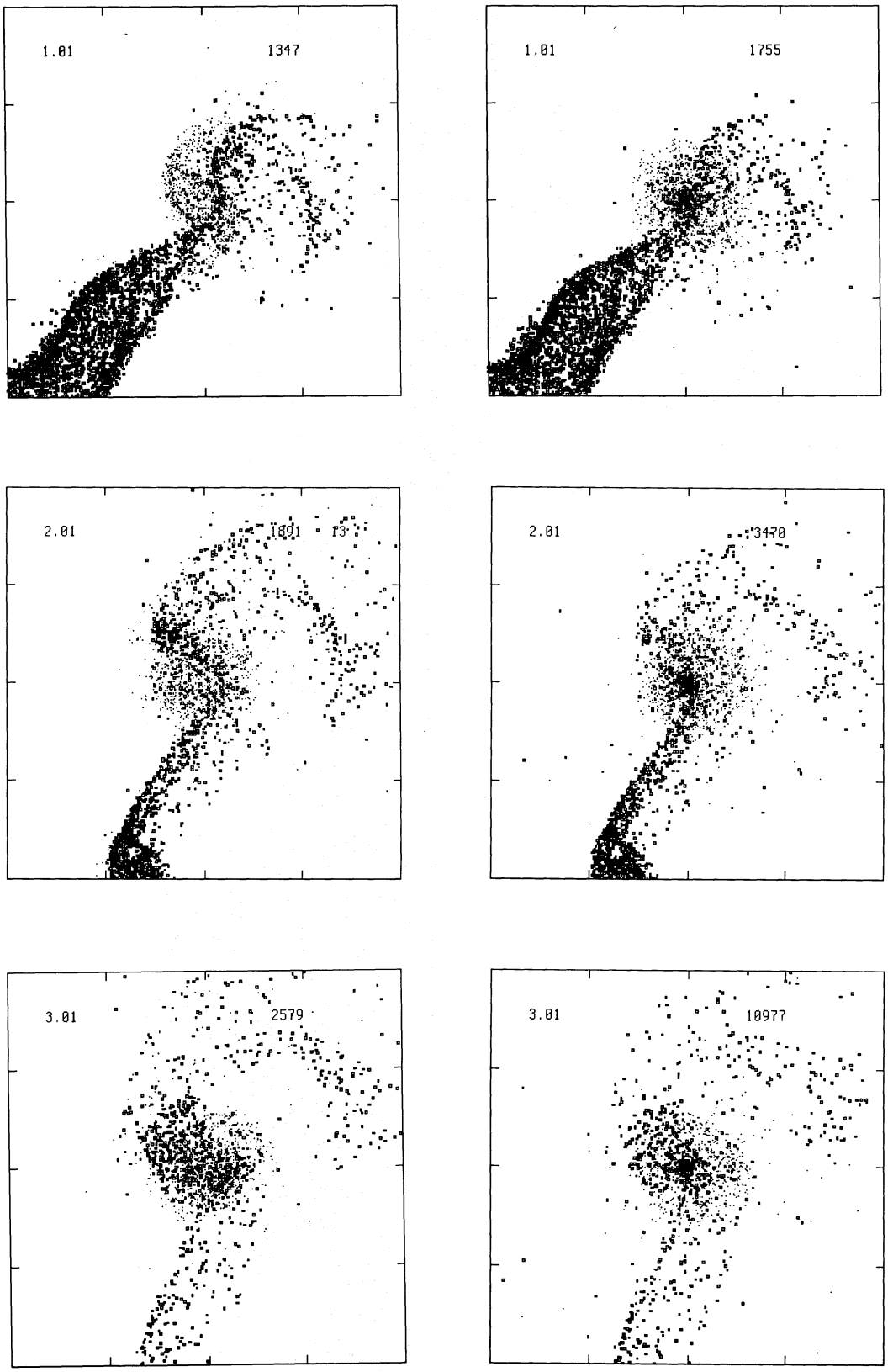

Fig. 11 (continued)

References

Brahic A., 1977, A&A 54, 895
Bushouse H.A., 1987, ApJ 320, 49
Byrd G.G., Valtonen M.J., Sundelius B., Valtaoja L., 1986, A&A 166, 75
Combes F., Gerin M., 1985, A&A 150, 327
Combes F., 1987, in: Galactic and Extragalactic Star Formation, eds. R.E. Pudritz, M. Fich, Kluwer London New York, p. 475
Cutri R.M., McAlary C.W., 1985, ApJ 296, 90
Dahari O., 1984, AJ 89, 966
Dahari O., 1985, ApJS 57, 643
Joseph R.D., Wright G.S., 1985, MNRAS 214, 87
Hämeen-Anttila K.A., Lukkari J., 1980, Ap&SS 71, 475
Kennicutt R.C., Keel W.C., 1984, ApJ 279, L5
Larson R.B., 1987, in: Galactic and Extragalactic Star Formation, eds. R.E. Pudritz, M. Fich, Kluwer, London New York, p. 459
Latanzio J.C., Henriksen R.N., 1988, MNRAS 232, 565
Laurikainen E., Moles M., 1989, ApJ 345, 176
Miller R., 1976, J. Comp. Phys 21, 400
Noguchi M., 1987, MNRAS 228, 635
Noguchi M., 1988, A&A 203, 259
Noguchi M., Ishibashi S., 1986, MNRAS 219, 305
Ostriker J.P., Peebles P.J.E., 1973, ApJ 186, 467
Roberts W.W., Hausman M.A., 1984, ApJ 237, 404
Salo H., 1985, Earth, Moon and Planets 33, 189
Salo H., 1987, Icarus 70, 37
Sellwood J.A., 1981, A&A 99, 362
Sellwood J.A., 1985 MNRAS 217, 127
Sellwood J.A., 1986, in: Use of Supercomputers in Stellar Dynamics, eds. S. McMillan, P. Hut, Springer, Berlin Heidelberg New York
Sellwood J.A., 1989, MNRAS 238, 115
Schwarz M.P., 1984, MNRAS 209, 93
Struck-Marcell C., Scalo J.M., 1987, ApJS 64, 39
Sundelius B., Thomasson M., Valtonen M.J., Byrd G.G., 1987, A&A 174, 67
Thomasson M., 1987, in: "The Few Body Problem", IAU Coll. 96, ed. M. Valtonen, Kluwer, Dordrecht, p. 387
Thomasson M., Donner K.J., Sundelius B., Byrd G.G., Huang T.-Y., Valtonen M.J., 1989, A&A 211, 25
Wisdom J., Tremaine S., 1988, AJ 95, 925
White R.L., 1988, ApJ 330, 26